DEM Simulations of a Bio–Inspired Site Characterization Probe with Two Anchors

Yuyan Chen[1], Alejandro Martinez[1], Jason DeJong[1]

[1]Civil and Environmental Engineering, University of California Davis, Davis CA, USA

Yuyan Chen: yych@ucdavis.edu
Alejandro Martinez: amart@ucdavis.edu (*corresponding author)
Jason DeJong: jdejong@ucdavis.edu

Abstract

Insufficient reaction force generated by installation equipment is one of the main challenges in soil penetration processes, which can lead to refusal conditions or pullout failures during in–situ testing, soil sampling, and pile driving. Recent research has focused on developing probes for site characterization that can generate the reaction force required for probe insertion without external equipment. This study presents the results of 3D discrete element modeling (DEM) simulations of probes with single or dual anchors performed in a virtual calibration chamber (VCC) that applies a constant overburden pressure of 100 kPa. Following penetration of the probe to the desired depth, the anchors are expanded and then a single tip advancement stage is simulated using either displacement–controlled or force–limited motion. The simulation results indicate that dual–anchor probes generate greater capacities than single–anchor probes due to the mobilization of additional bearing forces. However, the capacity per anchor increases with increasing inter–anchor spacing due to the development of an active zone below the leading anchor which produces a decrease in effective stresses around the trailing anchor. During expansion of the anchors, the penetration resistances decrease due to the alteration of stresses around the probe tip. The simulation results are used to define a dimensionless 3D space to determine the combination of probe configurations that enable self–penetration; these configurations include greater inter–anchor spacings, smaller anchor–tip distances, and greater anchor expansion magnitudes.

1 Introduction

The process of soil penetration is ubiquitous in geotechnical engineering design and construction, necessary for activities such as soil sampling, drilling, excavation, pile driving, and tunneling. Soil penetration can present a number of challenges in geotechnical problems, including (i) the need to generate sufficient reaction force to overcome the soil penetration resistance in shallow stiff layers (i.e. hardpans, gravels) and at greater depths, (ii) the need to have access routes for the site investigation equipment (i.e. 20-ton CPT truck, drill rig) to reach certain testing location (i.e. toe of a dam, forested, remote, or urban areas), and (iii) the significant environmental impact to civil engineering projects (Raymond et al [45], Purdy et al [43]). While there are current solutions for penetrating soils with light equipment (i.e. Jol [20]; Navarrete et al. [37]), there is a motivation to develop tools that provide measurements commonly used in geotechnical design practice, such as the Cone Penetration Test (CPT) tip resistance, Pressuremeter (PMT) limit pressure, Dilatometer (PMT) pressures, or shear wave velocity.

Recent research has investigated the burrowing strategies employed by animals and plants in search of solutions to overcome the challenges associated with soil penetration processes. For example, Dorgan [17] provides a description of the strategies used by different animals to burrow in cohesive and non–cohesive soils from a biological perspective while Martinez et al. [29] provides a summary of the geomechanical processes involved in the burrowing of tree root systems, caecilians, razor clams, and earth and marine worms. Additional information regarding the biological aspects of animal and plant burrowing, such as anatomical and energetic constraints, can be found in [6, 23, 33, 47, 48, 54–57].

In the field of geotechnical engineering, some studies have explored bioinspired foundation and anchorage systems. For example, O'Hara and Martinez [38] and Martinez and O'Hara [31] performed laboratory and centrifuge tests on the snakeskin–inspired surfaces and piles, which exhibited interface friction directionality. Zhong et al. [65] analyzed the soil deformations and load transfer induced by snakeskin–inspired piles using 2D DEM simulations. Also, Mallett et al. [26] investigated the soil deformation patterns and quantified the failure mechanisms around tree root-inspired anchors, Burrall et al. [9] performed pullout tests on the orchard trees which indicated that root systems are 6 to 10 times more material efficient than conventional pile system, and Anselmucci et al. ([3] and [4]) used X-ray computed tomography to quantify the deformations around roots growing in sandy soil.

Previous numerical studies have investigated the behavior of bio–inspired probes and probe components with the goal of identifying configurations and strategies that allow a probe to generate the reaction force needed to overcome the soil penetration resistance. This concept is referred to as self–penetration or self–burrowing throughout this paper, and has been investigated in probes composed of an expandable anchor and a tip (i.e. employing the anchor–tip strategy). For example, Huang and Tao [19] performed 3D DEM penetration simulations to conclude that

that less energy was required for soil penetration subsequent to anchor expansion in comparison to direct penetration. Chen et al. [13] and Ma et al. [24] used DEM simulations to show that expansion of an anchor produced a reduction in the penetration resistance, while Chen et al. [14] explored the geomechanical processes that lead to such reduction in penetration resistance, which include arching and rotation of principal stresses. Martinez et al. [30] used cavity expansion in combination with data from field tests to conclude that dense sands represent the greatest challenge for self–penetration in probes that employ the anchor–tip strategy.

Researchers have developed laboratory–scale prototypes to evaluate burrowing performance. Cortes and John [16] performed penetration tests on a miniature cone penetration probe that has a balloon near the cone tip and showed that reduction in penetration resistance takes places when the balloon is inflated. Ortiz et al. [39] performed horizontal constant–force penetration tests using a soft robot to show that radial body expansion in combination with lateral tip oscillations facilitated a greater distance of penetration. Tao et al. [53] developed a soft robotic prototype which was able to burrow up to the soil surface by cyclic elongation–contraction motion. Borela et al. [7] used an X–ray CT scan to show that more robust anchorage and a greater tip advancement are achieved in loose sand than in dense sand. Naclerio et al. [34] developed a root–like robot that uses tip extension to reduce the friction along the shaft and air fluidization to reduce the soil penetration resistance.

The above studies illustrate the challenges associated with generating sufficient anchorage forces to overcome the soil penetration resistance, which has limited the deployment of the experimental prototypes developed to date to shallow soil conditions (i.e. smaller than 50 cm). The majority of these studies have focused on enabling self–penetration by decreasing the penetration resistance [13, 16, 24, 34, 39], while less attention has been placed on increasing the magnitude of anchorage that can be generated. Deployment of multiple anchors can be used as a strategy to improve the anchorage capacity; in fact, organisms such as earth and marine worms that employ peristalsis locomotion deploy multiple anchorage points along their body.

The goal of this paper is to explore the anchorage capacity and tip advancement ability of a bio–inspired probe that deploys two anchors in conditions relevant to geotechnical site characterization. This is done by means of 3D DEM simulations of the penetration process of probes with two anchors arranged in different configurations in a virtual calibration chamber (VCC) that applies k_0 conditions with an overburden pressure of 100 kPa to the granular assembly. Detailed analysis is presented on the interactions between the two anchors, the interactions between the anchors and the tip, and the anchor configurations that best enable self–penetration.

2 Model description

The DEM simulations are performed using the PFC 3D software (Version 5.0, Itasca). The model consists of a virtual calibration chamber, a probe, and particles (Fig. 1a). The VCC is simulated by a top wall, a bottom wall, and 12 radial ring walls, which together create a chamber with a diameter ($D_{chamber}$) of 0.7 m and a height ($H_{chamber}$) of 1.2 m. All boundary walls are servo–controlled to apply a constant stress boundary condition with the vertical and radial confining stresses equal to 100 kPa and 50 kPa, respectively (i.e. $K_0=\sigma'_r/\sigma'_v=0.5$). The radial ring walls are used to maintain a uniform distribution of radial boundary stress along the chamber height as shown in Fig. S1. The probe has a diameter (D_{probe}) of 0.044 m and an apex angle of 60°, which are equivalent to the values in a 15 cm^2 cone penetration test (CPT) probe. The granular assembly contained in the VCC is poorly–graded and consists of about 200,000 spherical particles with a mean diameter (D_{50}) of 0.0144 m, a coefficient of uniformity (C_U) of 1.2, and a coefficient of curvature (C_C) of 0.96. The assemblies are prepared to an initial void ratio of 0.61. More detailed information regarding the grain size distribution of the granular assembly and the specimen creation procedure can be found in Chen et al. [13,14].

The simulated particles were upscaled to reduce the computational cost, as is commonly done in DEM simulations. When upscaling particle sizes, it is important to ensure that the relative dimensions between the chamber, probe, and particles are reasonable to prevent particle size effect. The chamber–to–probe ($D_{chamber}/D_{probe}$) and probe–to–particle (D_{probe}/D_{50}) diameter ratios in this study are 15.9 and 3.1, respectively. Previous studies such as [5, 8, 10, 11, 13, 21, 62, 63] have demonstrated that $D_{chamber}/D_{probe}$ and D_{probe}/D_{50} ratios between 10.5 and 16.6 and between 2.7 and 4.4, respectively, allow for minimized particle scale and chamber size effects to properly simulate penetration problems in 3D DEM simulations. Detailed discussion regarding scale effects can be found in [13, 14, 21]. The simulation parameters were taken from Chen et al. [13, 14], which are listed in Table 1. Soil particle interactions are modeled using a linear contact model with rolling resistance, where the particle normal stiffness is proportional to its diameter ($k_n/d=10^8$ N/m^2) and the normal–to–shear stiffness ratio (k_n/k_s) is 1.5. The sliding and rolling friction coefficients (μ and μ_{rr}) are 0.4, where the μ_{rr} provides a resistance to particle rotations which simulates the interlocking effect of particle angularity [1, 59]. The particle–anchor friction coefficient (μ_p) is 0.3, which is similar to that measured experimentally for conventional CPT friction sleeves [28]. The particle and boundary wall friction coefficient (μ') is set to be 0.1 to ensure numerical stability in the simulation. In a vertical 'r–z' plane (Fig. 1b), 628 measurement spheres with a diameter (D_{MS}) of 0.033 m are uniformly distributed to measure soil stresses. The measurement sphere–to–mean particle volume ratio is about 12.0.

The modeling parameters were chosen such that the simulated particle assembly exhibits a behavior typical of coarse–grained soils. While a detailed discussion regarding the selection of the simulation parameters can be found in [13, 14, 22], select results of triaxial compression simulations under four different confining stresses are plotted in Fig. 2a–c to highlight the response of the assemblies. The triaxial result show expected sand–like soil behaviors: greater peak and residual deviatoric stresses (q), smaller peak stress ratios (q/p'), and smaller dilatancy are mobilized for specimens confined under higher vertical stress. In addition, the stress ratios at large axial strains reach a unique, critical state value. In addition, penetration resistance (q_c) friction sleeve (f_s) measurements, as well as Soil Behavior Type (SBT) classification [46], at varying overburden stresses show that the simulated granular assembly exhibits a penetration behavior characteristic of medium dense coarse–grained soils. This data is not included here for the sake of brevity; a detailed description of the results and trends can be found [13].

Fig. 3a depicts the simulated probe, which can be configured with one or two anchors. The probe configuration is characterized by anchor length (L), inter–anchor spacing (S), anchor–tip distance (H), and anchor expansion magnitude (EM). Each complete simulation models three stages: initial direct pushing stage termed cone penetration (CP), followed by expansion of the anchor(s) (AE), and then by tip advancement (TA), as shown in Fig. 3b. During CP stage the probe is displaced downward into the soil at a constant speed of 0.2 m/s to a depth of 0.9 m, during which the mobilized tip resistance (q_c) and sleeve friction (f_s) are calculated as follows:

$$q_c = \frac{4\sum_{i=1}^{N} Q_{ztip,i}}{\pi D_{probe}^2} \quad (1)$$

$$f_s = \frac{\sum_{i=1}^{N} Q_{zsleeve,i}}{L_{sleeve}\pi D_{probe}} \quad (2)$$

where $Q_{ztip,i}$ is the vertical component of the contact force i acting on the probe tip, $Q_{zsleeve,i}$ is the vertical component of the contact force i acting on the friction sleeve whose length (L_{sleeve}) of 0.16 m is equal to that of a CPT friction sleeve, and N is the total number of vertical contact forces acting on the tip or sleeve. All simulations begin with the same CP stage to ensure the same initial conditions for the AE and TA stages for all simulations.

During the AE stage, the anchor(s) are radially expanded at a rate of 0.2% per second of the probe's initial diameter (*D*=0.044 m) until the target *EM* is achieved, where *EM* is defined as:

$$EM = \frac{D_{anchor}}{D_{probe}} - 1 \quad (3)$$

During this stage, the radial and bearing anchor pressures (P_a and P_b) and the radial and bearing anchor forces (F_n and F_b) (Fig. 3b) are related as follows:

$$F_{n(j)} = \pi P_{a(j)} L D_{anchor} \quad (4)$$

$$F_{b(j)} = \frac{\pi}{4} P_{b(j)} (D_{anchor}^2 - D_{probe}^2) \quad (5)$$

where D_{anchor} is the anchor diameter after expansion and the subscript *j* only exists for dual anchor probes with *j*=1 representing the top anchor and *j*=2 representing the bottom anchor. The distance between the anchor and tip was varied between $0.5D_{probe}$ and $6D_{probe}$ equivalents, based on the results from Chen et al. (2021) that indicated that an H of $4D_{probe}$ equivalents is the maximum distance that allows for self-penetration. The close proximity between the anchor and the tip will have an important effect on the CPT f_s measurement; therefore, the f_s measurement was not recorded during the AE and TA stages.

In the TA stage, the anchors are displaced upward and the tip is displaced downward using a displacement–controlled algorithm or a velocity–controlled algorithm with force limits (referred to as force-limited algorithm) (Fig. 3c). During the displacement–controlled simulations, the probe anchor(s) and tip are displaced upward and downward, respectively, at a constant velocity of 0.2 m/s. During the force-limited simulations, a target force (F_{target}) is used to decide which of the probe sections is displaced at a constant velocity of 0.2 m/s. When either probe section (i.e. tip or anchor) mobilizes the F_{target} magnitude, it is assigned a velocity of zero. Once both probe sections mobilize F_{target}, the F_{target} is increased by 50 N (i.e. ΔF = 50 N). The F_{target} has an initial value of 50 N and the ΔF magnitude was determined based on a calibration exercise showing that the simulation results are insensitive to ΔF as long as it is smaller than 100 N. It is noted that the anchor force and the tip resistance force are not always equal during the TA stage but they reach equal values at the end of each loading increment. In either displacement-controlled or force-limited simulations, the TA stage is stopped once a tip displacement of 15 cm or an anchor displacement of 4 cm are reached. This tip displacement limit was chosen based on previous simulations on single anchor probes (Chen et al. 2021) showing that tip resistance is fully or nearly remobilized during the TA stage at displacements smaller or equal to 4 cm. During the TA stage, the overall length of the probe increases due to the movement in opposite directions of the tip and anchor. This is accommodated by an inner wall located between the anchor and tip which avoids particles from moving inside the probe. The properties assigned to this wall are the same as for the remaining of the probe.

During the TA stage, the bearing anchor force (F_b), friction anchor force (F_a), tip resistance force (Q_c), and sleeve friction force (Q_s) are calculated using Eqs. 5–8.

$$F_{a(j)} = 2\pi\, P_{a(j)}\, L\, D_{anchor}\, \mu_p \tag{6}$$

$$Q_c = \frac{\pi}{4}\, q_c\, D_{probe}^2 \tag{7}$$

$$Q_s = \pi\, f_{st}\, D_{probe} \tag{8}$$

where f_{st} is the average shear stress along the probe shaft.

The total reaction force (F_t) and total resistance force (Q_t) are then calculated as follows:

$$F_t = \sum_{j=1}^{N_a} \left[F_{a(j)} + F_{b(j)}\right] \tag{9}$$

$$Q_t = Q_c + Q_s \tag{10}$$

where N_a is the number of anchors.

The simulations remain in a quasi–static condition throughout the CP, AE, and TA stages, as evidenced by the inertial numbers (I) which are between 2.1×10^{-5} and 7.2×10^{-4}. These values satisfy the criteria ($I \leq 10^{-3}$) for maintaining quasi–static conditions [15, 42, 44]. In addition, the stiffness used for the simulations ensure that inter–particle overlaps of 99% of the particles are smaller than 1% of the particle radii.

This study simulated the self–penetration processes of 49 bio–inspired probes to explore the effects of the number of anchors, *S*, *H*, *EM*, and the control algorithm on the anchor capacity and self–penetration ability. As listed in Table 2, each simulation is named by the anchor configuration and control algorithm. For example, the designation 'H4S1EM0.5_D' refers to a probe with an anchor–tip distance *H* equivalent to 4 D_{probe} (i.e. H = 4D_{probe} = 0.176 m), inter–anchor spacing *S* equivalent to 1 D_{probe}, anchor expansion magnitude of 0.5, and which uses displacement–controlled motion. It is noted that to accommodate *S* values between 1 and 6 D_{probe} within the VCC, *L* had to be limited to 2 D_{probe} for the probes with two anchors. The two reference simulations performed with one anchor have an *L* of 2 D_{probe} and 4 D_{probe} and are named H4L2EM0.5_D and

H4L4EM0.5_D, with L designated in place of S as compared to the name of simulations with two anchors.

3 Results

Results obtained during the CP, AE, and TA stages are presented in this section. The CP stage provides results similar to those obtained during CPT soundings, consisting of q_c and f_s readings. The anchor capacities and the interactions between the anchors and the probe tip during the AE and TA stages are analyzed in terms of the forces acting on the probe sections as well as in terms of soil stresses and particle displacements around the probes. Lastly, the forces acting on the probe are used to map the effects of *S*, *H*, and *EM* on its self–penetration ability. The three stages simulated in this study are used to investigate the soil response and the feasibility of using one or two anchors to generate sufficient reaction forces to overcome the penetration resistance at an overburden pressure of 100 kPa.

3.1 Cone penetration stage

During the cone penetration stage, the probe is displaced downward into the VCC to a depth of 0.9 m. The profiles of measured q_c and f_s are plotted in Fig. 4a and b. The depth for the q_c profile corresponds to the tip location, while the depth for the f_s profile corresponds to the mid–point of the sleeve. As the probe is advanced into the specimen, the q_c and f_s increase gradually to relatively constant values with averages of 4.8 MPa and 30 kPa, respectively. The q_c and f_s values are used to calculate normalized tip resistance (Q_{tn}) and friction ratio (F_r) values of 47.3 and 0.62%, respectively. When plotted in the SBT chart by Robertson [46] (Fig. 4c), the CPT response indicates a material that is in the transition between contractive and dilative, which is consistent with medium–dense material density and the high effective stress magnitudes near the tip (Fig. S2). Chen et al. [13] provides more detailed results indicating that the DEM model simulates the penetration behavior of medium–dense sands across a range of overburden stresses between 25 and 400 kPa.

3.2 Anchor expansion stage

In this section, the results of simulations on two probes with a single anchor (simulations #1–2) and on seven probes with two anchors (simulations #3–9) are presented to investigate the effects of inter–anchor spacing on the anchor capacity on probes with an H of $4D_{probe}$, *EM* of 0.5 and L of $2D_{probe}$.

During the AE stage, the anchors are radially expanded at a constant rate. The evolution of the normal radial anchor force and tip resistance force of the two single–anchor probes and two dual–anchor probes are shown in Fig. 5a and 5b. The single anchor in the simulation H4L2EM0.5_D has the same length (L=$2D_{probe}$) as those in the simulations with two anchors, while the single anchor in the simulation H4L4EM0.5_D has twice the anchor length. The S in the dual–anchor simulations is varied between $1D_{probe}$ and $6D_{probe}$. The evolution of corresponding radial anchor forces F_n are shown in Fig. 5a–d. The single–anchor probes with L of $4D_{probe}$ and $2D_{probe}$ mobilize F_n values of 27.5 and 16.5 kN, respectively, corresponding to anchor pressures of 753 and 904 kPa. The anchor with a greater length mobilizes a smaller P_a likely because as the anchor length is increased the failure mechanism becomes more cylindrical in shape, and expanding a cylindrical cavity requires a smaller pressure than expanding a spherical cavity [2, 52, 61]. The two anchors of a given probe generate similar F_n values; however, the anchor spacing has an influence on F_n. Namely, the smallest and largest anchor spacings (S of $1D_{probe}$ and $6D_{probe}$) mobilize average F_n values of 12.5 kN and 15 kN, respectively, corresponding to P_a of 685 kPa and 822 kPa.

The magnitude of Q_c decreases as the anchors are expanded. As shown in Fig. 5e–h, Q_c decreases from an initial value of 7.2 kN to values of 6.05 kN and 5.07 kN for the probes with single anchors with L of $2D_{probe}$ and $4D_{probe}$, respectively, and to values of 5.4 kN and 6.0 kN for probes with two anchors with S of $1D_{probe}$ and $6D_{probe}$. Similar effects on the penetration resistance have been reported by previous studies. For example, Huang and Tao [19] showed an average reduction in tip resistance of 11.9%, Ma et al. [24] reported an initial increase in tip resistance due to soil compaction when inflating a balloon–shaped anchor which was followed by a subsequent decrease in tip resistance during anchor deflation, and Chen et al. [13, 14] illustrated that the reduction in Q_c is due to an increase in void ratio and tensile vertical strains induced near the cone tip due to anchor expansion.

The results described above indicate that the dual anchor probe with an S of $1D_{probe}$ mobilizes a similar P_L magnitude and a similar Q_c reduction as the single anchor simulation with L of $4D_{probe}$, implying that the proximity of the two anchors in the former results in a behavior similar to that of a single, longer anchor. On the other hand, the simulation with two anchors with S of $6D_{probe}$ mobilizes similar P_L and Q_c as the single anchor probe with L of $2D_{probe}$, suggesting that each anchor in the widely–spaced dual–anchor (S = 6 D_{probe}) simulation behaves in a near–isolated manner.

The trends of the anchor capacities can be further explored using particle– and meso–level quantities obtained from the DEM simulations, such as particle displacements and soil stresses. Spatial maps of particle displacements and soil stresses during the AE stage are presented in Figs. 6 and 7, respectively.

In the particle displacement maps, each particle's color is proportional to the magnitude of its displacement. The figures present results for the two single–anchor probes and four dual–anchor probes with varying S while H and EM are fixed at 4D_{probe} and 0.5, respectively. For the single–anchor simulations, the probe with the shorter anchor exhibits a more spherical–shaped failure zone (Fig. 6a) whereas the probe with the longer anchor exhibits a more cylindrical–shaped failure zone (Fig. 6b). These results are in qualitative agreement with the fact that the shorter anchor mobilized a greater anchor pressure. For the dual–anchor simulations, as the anchor spacing is increased from 1D_{probe} to 6D_{probe}, the soil particle displacements between the two anchors decrease and the failure mode changes from one that encompasses a single zone around both anchors for the simulation with S of 1D_{probe} to two individual failure zones for the simulation with S of 6D_{probe} (Fig. 6c–f).

Spatial maps of stress magnitudes and changes in stresses as a result of AE were generated. The soil stresses are obtained from the measurement spheres shown in Fig. 1b. The σ_r' and σ_v' maps at the end of the CP stage are included in Fig. S2 for reference. Only radial stress maps for the end of the AE stage are provided for select probes in Figs. S3. To better visualize the effects of each stage, changes in radial ($\Delta\sigma_r'$) and vertical ($\Delta\sigma_z'$) stresses are calculated at each measurement sphere. For the AE stage, $\Delta\sigma_k' = \sigma_{k,AE}' - \sigma_{k,CP}'$, and for the TA stage, $\Delta\sigma_k' = \sigma_{k,SP}' - \sigma_{k,AE}'$, where $\sigma_{k,CP}', \sigma_{k,AE}'$, and $\sigma_{k,SP}'$ are the stresses component at the end of the CP, AE, and TA stages, respectively, and k is either the vertical (z) or radial (r) direction.

During the AE stage, the stresses around the anchor increase while the stresses above and below the anchor and around the tip decrease, as shown in the stress change maps for the single–anchor probe (Fig. 7a and e). These stress maps reflect the mobilization of the radial anchor force and the reduction of tip resistance force, as previously shown in Fig. 5a and e and as described in detail in Chen et al. [13]. For dual–anchor probes, the stresses surrounding the anchors of the dual–anchor probes with S of 1D_{probe}, 4D_{probe}, and 6D_{probe} increase while the stresses around the probes' tip decrease (Fig. 7b–d, f–h). Clear interactions between the anchors take place during AE for the probe with S=1D_{probe} at locations between the anchors (Fig. 7b, f). In fact, the stress change maps for this simulation are similar to that of the single anchor with an L of 4D_{probe} (Fig.7a, e), consistent with the corresponding particle displacement maps. As S is increased, the interactions between the anchors diminish. This is shown by the soil between the anchors which experiences a decrease in stress for the probes with S of 4D_{probe} and 6D_{probe} (Fig. 7c, d, g, h). The figures also show a greater decrease in stresses around the probe tip when S is 1D_{probe} (Fig. 7b, f compared to Fig. 7d, h), which explain the greater decrease in Q_c for smaller S shown in Fig. 5g, h.

The results of 19 simulations on probes with two anchors (simulations #3–#21) are used to further investigate the effects of the S, H, and EM on the anchor normal forces and penetration resistances during the AE stage. The S values are varied between 1D_{probe} and 6D_{probe}, the H values are either 1D_{probe} or 4D_{probe}, and the EM values are 0.3, 0.5, and 0.7.

Fig. 8a-f presents the change in F_n on the top and bottom anchors (F_{n1} and F_{n2}, respectively) and Q_c with increasing S/D_{probe} at the end of the AE stage for probes with varying H and EM. The dashed lines represent the values for the single–anchor simulations with L of 2D_{probe} and 4D_{probe} for comparison. Both F_{n1} and F_{n2} increase with increasing S/D_{probe} (Fig. 8a–d), indicating a decrease in the interaction between the anchors as S/D_{probe} is increased. At the same S/D_{probe}, F_{n1} and F_{n2} are largely independent of H (Fig. 8a, c). Conversely, the probes with greater EM mobilize greater F_{n1} and F_{n2} (Fig. 8b, d) due to the increase in anchor surface area with EM. The Q_c values at the end of AE increase as S is increased (Fig. 8e, f), indicating that both anchors interact with the tip for both H=1D_{probe} and H=4D_{probe} cases. In addition, greater reductions in Q_c occur for simulations with smaller H (Fig. 8e) and with greater EM (Fig. 8f).

3.3 Tip advancement stage

The evolution of total forces F_t and Q_t (Eqs. 9 and 10) and the corresponding component forces F_a, F_b, Q_c, and Q_s (Eqs. 5–8) during the displacement-controlled TA stage for the two single–anchor probes and two dual–anchor probes with S of 1D_{probe} and 6D_{probe} are plotted in Fig. 9a–h as a function of vertical displacement. The single anchor probes with L of 2D_{probe} and 4D_{probe} mobilize F_t forces (Fig. 9a, b) averaging 5.5 kN and 7.4 kN, respectively; the greater force mobilized by the latter is due to its larger surface area. At the end of the TA stage, the H4L4EM0.5_D probe generates an F_a of 4.0 kN while the H4L2EM0.5_D probe generates a F_a of

2.1 kN (Fig. 9e and f). Both probes mobilize a similar F_b with a magnitude around 3.4 kN as well as mobilize similar Q_t forces, averaging about 7.8 kN, over the last 0.01 m of displacement (Fig. 9a–d).

The dual–anchor probes mobilize greater F_t than the single–anchor probes due to the generation of bearing forces by the two anchors. The F_{a2} and F_{b2} components of the bottom anchor on the probe with an S of $6D_{probe}$ are greater than those for the probe with an S of $1D_{probe}$ by 70% and 66%, respectively. This highlights the effect of S on the mobilization of anchorage force. Both of these probes mobilize Q_t forces similar to those mobilized by the single–anchor probes. These Q_t values correspond to q_c values close to 4.8 MPa, which is in agreement with results from Chen et al. 2021 [13] indicating that the q_c magnitude remobilized to values close to those at the end of the CP stage. This suggests that the q_c measured at the end of the TA stage could be used to estimate soil engineering properties using established CPT procedures. The results presented in Fig. 9 (e-h) together with those in Chen et al. 2021 indicate that q_c tends to remobilize irrespectively of S.

The influence of S on the capacity of dual–anchor probes is further illustrated in Fig. 10a–c, which show the relationship between average F_a, F_b, and F_t obtained during the last 0.01 m of displacement with normalized spacing (S/D_{probe}). The dashed lines represent the values for the single–anchor simulations with L of $2D_{probe}$ and $4D_{probe}$ for comparison. The results indicate that the F_{a1} and F_{b1} (forces on the top anchor) are largely independent of S/D_{probe}, while the F_{a2} and F_{b2} (forces on the bottom anchor) increase with increasing S/D_{probe} (Fig. 10a, b). As shown in Fig. 10c, the total reaction force mobilized by the probes with two anchors ($F_t = F_{t1} + F_{t2}$) increases as S/D_{probe} is increased due to the increase in F_{t2}. In all instances, the F_t values for the dual–anchor probes are greater than those for the single–anchor probes. However, the F_t values for the two–anchor probes are smaller than twice the F_t value for the single–anchor probe with an L of $2D_{probe}$, indicating that while the capacity of two anchors is greater than the capacity of one, the efficiency of the former in terms of total capacity per anchor number is decreased. These results are consistent with those in previous numerical and experimental studies on helical anchors, which demonstrate the reduction in efficiency when the inter–helix spacing was smaller than 1.5 to 3 base diameter equivalents [18, 32, 36].

The spatial maps of particle displacements and soil stresses for single–anchor and double–anchor probes are presented to investigate the interaction effects during the TA stage. The particle displacement maps for the TA stage show that as the tip is displaced downward, significant particle displacements occur around and below the tip in a similar manner for all simulations (Fig. 11a–f). As the anchors are displaced upward, a 'butterfly–shaped' zone is formed around the anchors with the particles undergo large displacements. When the S is $1D_{probe}$, particle displacements greater than 10 mm are observed between the two anchors, indicating significant interactions between them (Fig. 11c, d). The shape of the disturbed zone between the single–anchor simulation with an L of $4D_{probe}$ and dual–anchor simulation with an S of $1D_{probe}$ is remarkably similar (Fig. 11b, c). In contrast, much smaller displacements (1 to 4 mm) between the two anchors are observed for the probe with an S of $6D_{probe}$ (Fig. 11f). This difference in failure mode for small and large spacings has also been analyzed in previous multi–plate anchors related topic. For example, Wang et al. [58] showed that a global 'cylindrical failure' in the incremental displacement fields occurred during the uplifting of two–plate anchors when spacing is smaller than 3 base diameter equivalents, while individual bearing failure mechanisms occurred when the spacing is greater than 5 base diameter equivalent. Additionally, Nally and Hambleton [36] showed that increasing the number of plate anchors gradually changed the soil failure mode from a 'passive' failure zone, which extend from bottom anchor to soil surface, to a uniform 'single–column' failure zone passing through all anchors. The smaller interactions in the DEM simulations between the anchors at larger S can help explain the previously discussed trends, including the convergence of F_{n1} and F_{n2} to the single–anchor case during AE and the convergence of F_{a1}, F_{a2}, F_{b1}, F_{b2}, F_{t1}, and F_{t2} to the single–anchor case during TA as S approaches $6D_{probe}$ (Figs. 8, 10).

The spatial stress difference maps at the end of the TA stage are shown in Fig. 12. The radial stresses at the end of the TA stage can be found in Fig. S4. During the TA stage, strong interactions occur between the anchors for the probe with an S of $1D_{probe}$. Namely, the stresses at locations immediately below the top anchor decrease while those at locations immediately above the bottom anchor increase, indicating development of active and passive zones within the particles (Fig. 12b, f). The active zone developed below the top anchor results in smaller stresses being mobilized around the bottom anchor in comparison with the simulations with an S of $4D_{probe}$ and $6D_{probe}$ (Fig. 12c, d, g, h), which is responsible for the smaller bearing and friction forces being mobilized by the bottom anchor, as shown in Fig. 10a–c. The stresses below the probe tip are comparable in all three simulations, indicating limited effects of spacing on the Q_c force.

The results of 19 simulations on probes with two anchors (simulations #3–#21) that have varying S, H, and EM are used to further investigate the interaction effects during the TA stages.

During the displacement–controlled TA stage, the forces on the anchors and tip change due to either stress relaxation or remobilization, as previously described. Namely, F_a decreases and F_b increases as the anchors are displaced upward and Q_c increases as the tip is displaced downward. Figure 13 presents the forces on the bottom anchor (F_{a2} and F_{b2}) and Q_c with increasing S/D_{probe} at the end of TA for different anchor configuration conditions. Only values for the bottom anchor are presented here because the forces on the top anchor were approximately independent of S/D_{probe}; a similar independence of top anchor capacity on spacing has been reported by Misir [32] in the finite element modeling of a shaft with two–plate anchors moving upward.

At the end of TA, F_{a2} increases as S/D_{probe} is increased. However, the results suggest that F_{a2} is independent of the H and EM values (Fig. 13a, b). F_{b2} also increases with increasing spacing (Fig. 13c, d) due to the decrease in the inter–anchor interactions. This observation is consistent with results from previous numerical and experimental pullout tests on multi–plate and multi–helix anchors [18, 32], which showed an increase in bottom anchor capacity and capacity per anchor with the increasing spacing. In the DEM simulations, the anchors with H of $4D_{probe}$ mobilize slightly greater F_{b2} than those with H of $1D_{probe}$, suggesting a small effect of the proximity to the probe tip. The anchors with EM of 0.5 and 0.7 mobilize greater F_{b2} than the anchors with EM of 0.3. However, F_{b2} values for the anchors with EM of 0.7 are slightly smaller than those for the anchor with EM of 0.5 (Fig. 13d), likely due to the stronger inter–anchor interactions resulting from the greater expansion magnitude. In addition, the probes with EM of 0.5 mobilize similar F_{a2} and F_{b2} values as the probe with a single anchor case when S is $6D_{probe}$, suggesting that the anchor interactions diminish at this large spacing (Fig. 13a, c). The Q_c forces at the end of TA appear to be independent of S/D_{probe}, although the values are smaller for simulations with a smaller H and greater EM (Fig. 9e, f).

3.4 Probe self-penetration potential

As previously discussed, probe self–penetration ability refers to the ability to mobilize greater total reaction forces than total resistance forces. For displacement–controlled simulations, the ratio of total reaction to total resistance forces (F_t/Q_t) can be used to evaluate the probe self–penetration ability, with F_t/Q_t values greater than 1.0 indicating successful self–penetration. Fig. 14 shows the F_t/Q_t ratios for all the displacement–controlled simulations (#3–21) at the end of TA, which indicate that simulations with an H of $1D_{probe}$ and EM of 0.7 have F_t/Q_t greater than 1.0 (black squares and yellow triangles). Simulations with greater *H* and smaller *EM* can have F_t/Q_t smaller than 1.0. For example, at spacings of $0.5D_{probe}$ to $2D_{probe}$, the simulations with an *H* of $4D_{probe}$ and *EM* of 0.5 (red circles) have an F_t/Q_t slightly smaller than 1.0, but at larger spacings the ratios are greater than 1.0. Also, the simulations with an *EM* of 0.3 (blue triangles) all have F_t/Q_t smaller than 1.0.

The ability of the probe to advance its tip can be further evaluated using separate force-limited motion (Fig. 3c). An additional series of 12 simulations (#22–32, 36, 37) was performed with the goal of evaluating the effect of *S*, *EM*, and *H* on the self–penetration ability of the dual–anchor probes. The force-limited algorithm allows for the probe section that mobilizes a total force smaller than F_{target} to be displaced at a constant velocity. Therefore, the tip advancement ability can be evaluated in terms of the self–penetration displacement ΔD:

$$\Delta D = |\delta_{tip}| - |\delta_{anchor}| \tag{12}$$

where δ_{tip} and δ_{anchor} are the displacement vectors of the tip and the anchor, and a positive ΔD indicates the achievement of self–penetration where the net tip displacement is towards greater depths. Figures 15a–c show time histories of ΔD for probes with different anchor configurations. Tip advancement is achieved by the probes with combinations involving *EM* greater than or equal to 0.5 and *S* greater than or equal to $4D_{probe}$. It is noted that the simulation 'S=$0D_{probe}$' corresponds to H4L4EM0.5_F (simulation #35), which can be considered as a dual–anchor probe with zero inter–anchor spacing. The horizontal axis in the plot is normalized time ($\bar{t}$), which is defined as the time within the TA stage normalized by the total duration of the TA stage.

To explore the probe configurations that enable self-penetration, an additional series of 18 simulations (#33–50) were performed. In total, the results of 48 simulations using either displacement–controlled or force-limited motion are plotted in a dimensionless 3D space defined by *EM*, H/D_{probe}, and S/D_{probe} (Fig. 16). In the figure, the black datapoints indicate the probe configurations that achieved self-penetration and the red datapoints represent the probe configurations that did not achieve self-penetration, as defined by the conditions described above (F_t/Q_t greater than 1.0 or a positive ΔD during TA). As shown, the result of the displacement-controlled and force-limited simulations are in agreement. The configurations that enable self–penetration include greater *EM*, smaller H/D_{probe}, and greater S/D_{probe}, as previously described. Using least square fitting, a plane that separates the configurations that achieved self–penetration from those that failed is identified, which is defined by $EM = -0.046 * S/D_{probe} + 0.020 *$

$H/D_{probe} + 0.488$. In this equation, the negative –0.046 coefficient indicates that a smaller EM is required for probes with greater S to achieve self–penetration, while the positive 0.020 coefficient indicates that a greater EM is needed for probes with greater H to achieve self–penetration. Lastly, the 0.488 constant indicates the minimum EM value that would be required to achieve self–penetration if both H and S are zero. It is noted that it is likely that the plane that separates successful from unsuccessful self-penetration is dependent on the length of the anchors; particularly, the plane is expected to move downward as the anchor length is increased.

4 Implications and limitations

The results presented in this paper cover a limited number of conditions, including probes with one or two anchors, anchor lengths equivalent to 2 or $4D_{probe}$, and soil conditions that simulate a medium–dense coarse–grained soil under an overburden stress of 100 kPa, equivalent to a depth of about 10 m of saturated soil or 5 m of dry soil. The trends reported here should be verified using physical experiments across a range of overburden stresses as well as for coarse–grained soils with smaller particles, well–graded coarse soils, and fine–grained soils.

Another aspect that needs to be examined is the possible effect of the particle size on the simulation results, in particular with regard to the interaction between the particles and the anchor's bearing area. In the simulations presented in this paper, a D_{probe}/D_{50} of 3.1 was employed,and the ratio of the length of the anchor bearing area to the median particle size ($(D_{anchor}$-$D_{probe})/2D_{50}$) was 0.8. To explore possible particle size effects, a specimen with the same model parameters (Table 1) that employs the particle refinement method (McDowell et al 2012) was generated to decrease the size of the particles contacting the probe. Specifically, these particles had a D_{50} of 6.3 mm, which produces a D_{probe}/D_{50} of 7.0 and $((D_{anchor}$-$D_{probe})/2D_{50}$ of 1.7. This specimen contains five different zones, as shown in the model illustration and particle size distributions in Figure S5. An additional displacement-controlled simulation with a single-anchor probe with H = $4D_{probe}$ and L= $2D_{probe}$ was performed on this specimen. A comparison of the results with those from the original specimen is provided in Table 3 and Figure S6. In summary, the difference in the average q_c and f_s in the CP stage are 8.3% and 13.7%, respectively. At the end of the AE stage, there is a difference of 14.5% and 8.2% in the F_n and Q_c values, and at the end of the TA stage there is a difference of 11.0% and 11.8% in the F_t and Q_t values. While in general the forces are greater for the specimen with smaller particles, the differences are smaller than 15% and the final result was the same in both simulations, with tip advancement failing. Therefore, it can be concluded that while there may be a small dependency of the magnitude mobilized forces on the particle size, the conclusions of the simulations are unaffected.

Despite the aforementioned potential limitations, the results presented in this study can help in understanding the processes that produce the interactions between the anchors and the tip, and the identification of the plane that separates probe configurations leading to successful and unsuccessful tip advancement can guide the design of future bio–inspired self–penetration probe prototypes. Previous studies have also explored the effects of other parameters. For example, Chen et al. [13] showed that the tip advancement ability of the probe increases with increasing anchor length. They also showed that the anchor reaction forces increase at a greater rate with increasing overburden stress than the penetration resistance forces, suggesting that tip advancement reaction becomes more feasible at greater depths. Finally, it can be expected that the reaction mobilized by a probe will increase as more anchors are deployed; however, it is likely that the capacity per anchor will decrease as more anchors are deployed.

5 Conclusions

3D DEM simulations of single and dual anchor bio–inspired probes were performed to evaluate the effects of the inter–anchor spacing, anchor–tip distance, and anchor expansion magnitude on the interactions between the anchors and the probe tip and on the probe's self–penetration ability. The simulations were performed in a virtual calibration chamber that applies constant vertical and radial stresses to the contained specimen to simulate the soil penetration process at an overburden stress representative of 10 m in saturated soil. Simulations were either performed with a displacement-controlled or a force-limited probe motion algorithm, and the final result of the simulation (i.e. self penetration versus anchor lifting) was unaffected by the choice of motion control.

The simulation results indicate that the dual–anchor probes outperformed the single–anchor probes due to the mobilization of two bearing resistance components. It is shown that the anchorage capacity increases with increasing inter–anchor spacing due to a reduction in detrimental interactions between the anchors. At an inter–anchor spacing equivalent to five or six times the probe diameter, the forces mobilized during anchor expansion and tip advancement converged to those mobilized by individual anchors. This takes place when near–isolated failure modes are developed around each anchor, where particle displacements and changes in stresses at locations between the anchors are small. The results indicate that the reaction forces mobilized by the top anchor are approximately independent of inter–anchor spacing. In contrast, the forces mobilized by the bottom anchor decreased as the inter–anchor spacing was decreased due to the formation of an active wedge below the top anchor, which caused a reduction in effective stresses around the bottom anchor. In agreement with previous simulations, expansion of the anchors resulted in a decrease in the penetration resistance. This reduction was also influenced by the probe configuration, where smaller inter–anchor spacings, smaller anchor–tip distances, and greater anchor expansion magnitudes led to greater reductions.

Simulations using the two probe motion algorithms indicate that the self–penetration ability of the probe is increased for the following conditions: (i) increasing the inter–anchor spacing due to the reduction of the detrimental anchor interactions, (ii) decreasing the anchor–tip distance due to the greater reduction in penetration resistance, and (iii) increasing expansion magnitude due to the greater anchorage capacity and greater reduction in penetration resistance. The simulation results were used to define a plane in 3 unitless dimensions (EM versus S/D_{probe} versus H/D_{probe}) that separates the anchor configurations that enable self–penetration from those that result in anchor lifting. This plane could be used to guide the design of future probe prototypes to be deployed in the laboratory and field.

Data availability statement

The datasets generated during and/or analyzed during the current study are available from the corresponding author on reasonable request.

Acknowledgement

This material is based upon work supported in part by the Engineering Research Center Program of the National Science Foundation under NSF Cooperative Agreement No. EEC–1449501. The first and second authors were supported by the National Science Foundation (NSF) under Award No. 1942369. Any opinions, findings, and conclusions or recommendations expressed in this material are those of the author(s) and do not necessarily reflect those of the National Science Foundation.

References

1. Ai J, Chen JF, Rotter JM, Ooi JY (2011) Assessment of rolling resistance models in discrete element simulations. Powder Technol 206(3): 269–282. https://doi.org/10.1016/j.powtec.2010.09.030
2. Ajalloeian R, Yu HS (1998) Chamber studies of the effect of pressuremeter geometry on test results in sand. Geotechnique 48(5):621–636. https://doi.org/10.1680/geot.1998.48.5.621
3. Anselmucci F, Andò E, Viggiani G, Lenoir N, Arson C, Sibille L (2021) Imaging local soil kinematics during the first days of maize root growth in sand. Scientific reports. 2021 Nov 15;11(1):1-3. https://doi.org/10.1038/s41598-021-01056-1
4. Anselmucci F, Andó E, Viggiani G, Lenoir N, Peyroux R, Arson C, Sibille L. Use of X-ray tomography to investigate soil deformation around growing roots. Géotechnique Letters. 2021 Mar;11(1):96-102. https://doi.org/10.1680/jgele.20.00114
5. Arroyo M, Butlanska J, Gens A, Calvetti F, Jamiolkowski M (2011) Cone penetration tests in a virtual calibration chamber. Géotechnique 61(6):525–31. https://doi.org/10.1680/geot.9.P.067
6. Barnett CM, Bengough AG, McKenzie BM (2009) Quantitative image analysis of earthworm–mediated soil displacement. Biol Fertil Soils 45(8):821–828. https://doi.org/10.1007/s00374–009–0392–9
7. Borela R, Frost JD, Viggiani G, Anselmucci F (2020) Earthworm–inspired robotic locomotion in sand: an experimental study using x–ray tomography. Geotech Lett 1(1):66–73. https://doi.org/10.1680/jgele.20.00085
8. Butlanska J, Arroyo M, Gens A, O'Sullivan C (2014) Multi–scale analysis of cone penetration test (CPT) in a virtual calibration chamber. Can Geotech J 51(1):51–66. https://doi.org/10.1139/cgj–2012–0476
9. Burrall M, DeJong JT, Martinez A, and Wilson, DW (2020). Vertical pullout tests of orchard trees for bio–inspired engineering of anchorage and foundation systems. Bioinspiration & Biomimetics, 16(1), p.016009. https://doi.org/10.1088/1748–3190/abb414
10. Ciantia MO, Arroyo M, Butlanska J, Gens A (2016) DEM modelling of cone penetration tests in a double–porosity crushable granular material. Comput and Geotech 73:109–127. https://doi.org/10.1016/j.compgeo.2015.12.001

11. Ciantia M, O’Sullivan C, Jardine R J (2019) Pile penetration in crushable soils: insights from micromechanical modelling. 17th European Conference on soil Mechanics and Geotechnical Engineering (ECSMGE 2019) International Society for Soil Mechanics and Geotechnical Engineering. https://doi.org/10.32075/17ECSMGE–2019–1111
12. Chapman G (1950) Of the movement of worms. J Exp Biol 27(1):29–39. https://doi.org/10.1242/jeb.27.1.29
13. Chen Y, Khosravi A, Martinez A, DeJong J (2021) Modeling the self–penetration process of a bio–inspired probe in granular soils. Bioinspir Biomim 16(4) 046012. https://doi.org/10.1088/1748–3190/abf46e
14. Chen, Y, Martinez A, DeJong J (2022) Alteration of the stress state around a bio–inspired probe enables self–penetration. Accepted by Can. Geotech. J. http://dx.doi.org/10.1139/cgj–2021–0260
15. Combe G, Roux JN (2009) Discrete numerical simulation, quasistatic deformation and the origins of strain in granular materials. arXiv preprint arXiv:0901.3842
16. Cortes D, John S (2018) Earthworm–inspired soil penetration. In the 1st Biomediated and Bioinspired Geotechnics (B2G) Conference. Atlanta, GA.
17. Dorgan KM (2015) The biomechanics of burrowing and boring. J Exp Biol 218(2):176–183. https://doi.org/10.1242/jeb.086983
18. Hao D, Wang D, O’Loughlin CD, Gaudin C (2019) Tensile monotonic capacity of helical anchors in sand: interaction between helices. Can Geotech J 56(10):1534–1543. https://doi.org/10.1139/cgj–2018–0202
19. Huang S, Tao J (2020) Modeling Clam–inspired Burrowing in Dry Sand using Cavity Expansion Theory and DEM. Acta Geotech 15:2305–2326. https://doi.org/10.1007/s11440–020–00918–8
20. Jol HM (2008) Ground penetrating radar theory and applications. elsevier; 2008 Dec 8. ISBN: 978-0-444-53348-7
21. Khosravi A, Martinez A, DeJong JT (2020) Discrete element model (DEM) simulations of cone penetration test (CPT) measurements and soil classification. Can Geotech J 57(9):1369–1387. https://doi.org/10.1139/cgj–2019–0512
22. Kuei KC, DeJong JT, Martinez A (2020). Particle size effects on the strength and fabric of granular media. GeoCongress 2020.

23. Kurth JA, Kier WM (2014) Scaling of the hydrostatic skeleton in the earthworm Lumbricus terrestris. J Exp Biol 217(11):1860–1867. https://doi.org/10.1242/jeb.098137
24. Ma Y, Evans TM, Cortes DD (2020) 2D DEM analysis of the interactions between bio–inspired geo–probe and soil during inflation–deflation cycles. Granul Matter 22(11). https://doi.org/10.1007/s10035–019–0974–7
25. McDowell GR, Falagush O, Yu HS. A particle refinement method for simulating DEM of cone penetration testing in granular materials. Géotechnique Letters. 2012 Sep 28;2(3):141-7. https://doi.org/10.1680/geolett.12.00036
26. Mallett SD, Siegel A, Vego I, Frost JD. Uplift behavior of root-inspired anchorage models. InProceedings of International Symposium on Bio-mediated and Bio-inspired Geotechnics, Atlanta 2018.
27. Mayne PW (2007) Cone penetration testing, 368. Transportation Research Board.
28. Martinez A, Frost JD (2017) The influence of surface roughness form on the strength of sand–structure interfaces. Géotechnique Letters 7(1):104–111. https://doi.org/10.1680/jgele.16.00169
29. Martinez, A., DeJong, J., Akin, I., Aleali, A., Arson, C., Atkinson, J., Bandini, P., Baser, T., Borela, R., Boulanger, R., Burrall, M., Chen, Y., Collins, C., Cortes, D., Dai, S., DeJong, T., Del Dottore, E., Dorgan, K., Fragaszy, R., Frost, D., Full, R., Ghayoomi, M., Goldman, D., Gravish, N., Guzman, I.L., Hambleton, J., Hawkes, E., Helms, M., Hu, D.L., Huang, L., Huang, S., Hunt, C., Irschick, D., Lin, H., Lingwall, B., Marr, W.A., Mazzolai, B., McInroe, B., Murthy, T., O'Hara, K., Porter, M., Sadek, S., Sanchez, M., Santamarina, C., Shao, L., Sharp, J., Stuart, H., Stutz, H.H., Summers, A.P., Tao, J., Tolley, M., Treers, L., Turnbull, K., Valdes, R., van Paassen, L., Viggiani, G., Wilson, D., Wu, W., Yu, X. and Zheng, J. (2021) Bio–inspired geotechnical engineering: principles, current work, opportunities and challenges. Géotechnique 1–19. https://doi.org/10.1680/jgeot.20.P.170
30. Martinez A, DeJong JT, Jaeger RA, Khosravi A (2020) Evaluation of self–penetration potential of a bio–inspired site characterization probe by cavity expansion analysis. Can Geotech J 57(5):706–716. https://doi.org/10.1139/cgj–2018–0864

31. Martinez A, O'Hara KB (2021). Skin friction directionality in monotonically-and cyclically-loaded bio-inspired piles in sand. Deep Found. Inst. J. 2021. https://dfi-journal.org/dfi/journal/pdfs/vol15no1martinez222.pdf
32. Misir G (2018) Predicting the uplift capacity of vertically located two–plate anchors. Acta Geotech Slov 15(2):47–57. https://doi.org/10.18690/actageotechslov.15.2.47–57.2018
33. Murphy EAK, Dorgan KM (2011) Burrow extension with a proboscis: mechanics of burrowing by the glycerid Hemipodus simplex. J Exp Biol 214:1017–1027. https://doi.org/10.1242/jeb.051227
34. Naclerio ND, Karsai A, Murray–Cooper M, Ozkan–Aydin Y, Aydin E, Goldman DI, Hawkes EW (2021) Controlling subterranean forces enables a fast, steerable, burrowing soft robot. Sci Robot 6(55). https://doi.org/10.1126/scirobotics.abe2922
35. Nakamura T, Kato T, Iwanaga T, Muranaka Y (2006) Development of a peristaltic crawling robot based on earthworm locomotion. J Robot Mechatron 18(3):299–304. https://doi.org/10.20965/jrm.2006.p0299
36. Nally A and Hambleton JP (2019) Assessment of analysis techniques for multi–plate anchors in sand. In Proceedings of the 44th Annual Conference on Deep Foundations.
37. Navarrete MA, Breul P, Gourvès R (2021). Application of wave equation theory to improve dynamic cone penetration test for shallow soil characterisation. Journal of Rock Mechanics and Geotechnical Engineering. 2021 Sep 7. https://doi.org/10.1016/j.jrmge.2021.07.004
38. O'Hara KB, & Martinez A (2020). Monotonic and cyclic frictional resistance directionality in snakeskin–inspired surfaces and piles. Journal of Geotechnical and Geoenvironmental Engineering, 146(11), 04020116. https://doi.org/10.1061/(ASCE)GT.1943–5606.0002368
39. Ortiz D, Gravish N, Tolley MT (2019) Soft Robot Actuation Strategies for Locomotion in Granular Substrates IEEE Robot. Autom Lett 4(3):2630–2636. https://doi.org/10.1109/LRA.2019.2911844
40. Quillin KJ (1999) Kinematic scaling of locomotion by hydrostatic animals: ontogeny of peristaltic crawling by the earthworm Lumbricus terrestris. J Exp Biol 202(6):661–674. https://doi.org/10.1242/jeb.202.6.661
41. Quillin KJ (2000) Ontogenetic scaling of burrowing forces in the earthworm Lumbricus terrestris. J Exp Biol 203(18):2757–2770. https://doi.org/10.1242/jeb.203.18.2757

42. O'Sullivan C (2011) Particulate Discrete Element Modelling: A Geomechanics Perspective. (CRC Press)
43. Purdy C, Raymond AJ, DeJong JT, Kendall A (2020) Life Cycle Assessment of Site Characterization Methods. InGeo-Congress 2020: Geo-Systems, Sustainability, Geoenvironmental Engineering, and Unsaturated Soil Mechanics 2020 Feb 21 (pp. 80-89). Reston, VA: American Society of Civil Engineers. https://doi.org/10.1061/9780784482827.009
44. Radjai F, Richefeu V (2009) Contact dynamics as a nonsmooth discrete element method. Mech Mater 41(6):715–728. https://doi.org/10.1016/j.mechmat.2009.01.028
45. Raymond AJ, Tipton JR, Kendall A, DeJong JT (2020) Review of impact categories and environmental indicators for life cycle assessment of geotechnical systems. Journal of Industrial Ecology. Jun;24(3):485-99. https://doi.org/10.1111/jiec.12946
46. Robertson PK (2010) Soil behaviour type from the CPT: an update. In 2nd International symposium on cone penetration testing (Vol. 2, pp. 575–583). Cone Penetration Testing Organizing Committee.
47. Ruiz S, Or D, Schymanski S J (2015) Soil penetration by earthworms and plant roots – mechanical energetics of bioturbation of compacted soils. PLoS One 10(6) e0128914. https://doi.org/10.1371/journal.pone.0128914
48. Sadava DE, Hillis DM, Heller HC, Berenbaum M (2009) Life: the science of biology (Vol. 2). Macmillan.ISBN: 978–4292–4647–7
49. Salgado R, Mitchell JK, Jamiolkowski M (1997) Cavity expansion and penetration resistance in sand. J Geotech Geoenviron 123(4):344–354. https://doi.org/10.1061/(ASCE)1090–0241(1997)123:4(344)
50. Salgado R, Prezzi M (2007) Computation of cavity expansion pressure and penetration resistance in sands. Int J Geomech 7(4):251–265. https://doi.org/10.1061/(ASCE)1532–3641(2007)7:4(251)
51. Savioli A, Viggiani C, Santamarina JC (2014) Root–soil mechanical interaction. In Geo–Congress 2014: Geo–characterization and Modeling for Sustainability, pp 3977–3984. https://doi.org/10.1061/9780784413272.386
52. Schnaid F (1990) A study of the cone–pressuremeter test in sand. PhD Thesis University of Oxford Schofield A N and Wroth C P 1968 Critical State Soil Mechanics McGraw–Hill.

53. Tao J, Huang S, Tang Y (2020) SBOR: a minimalistic soft self–burrowing–out robot inspired by razor clams. Bioinspir Biomim 15(5) 055003. https://doi.org/10.1088/1748–3190/ab8754
54. Trueman ER (1968) The burrowing activities of bivalves. Synp Zool Soc Lond 22:167–186.
55. Trueman ER (1968) A comparative account of the burrowing process of species of Mactra and of other bivalves. J Mollus Stud 38(2):139–151. https://doi.org/10.1093/oxfordjournals.mollus.a065032
56. Trueman ER (1968) Burrowing habit and the early evolution of body cavities. Nature 218:96–98. https://doi.org/10.1038/218096a0
57. Trueman ER (1968) The locomotion of the freshwater clam Margaritifera margaritifera (Unionacea: Margaritanidae). Malacologia 6:401–410.
58. Wang D, Merifield RS, Gaudin C (2013) Uplift behaviour of helical anchors in clay. Can Geotech J 50(6):575–584. https://doi.org/10.1139/cgj–2012–0350
59. Wensrich CM, Katterfeld A (2012) Rolling friction as a technique for modelling particle shape in DEM Powder Technol. 217:409–417. https://doi.org/10.1016/j.powtec.2011.10.057
60. Yu HS, Houlsby GT (1991) Finite cavity expansion in dilatant soils: loading analysis Geotechnique 41(2):173–183. https://doi.org/10.1680/geot.1991.41.2.173
61. Yu HS, Schnaid F, Collins IF (1996) Analysis of cone pressuremeter tests in sands J. Geotech. Eng. 122(8):623–632. https://doi.org/10.1061/(ASCE)0733–9410(1996)122:8(623)
62. Zeng Z, Chen Y (2016) Simulation of soil–micropenetrometer interaction using the discrete element method (DEM). Trans ASABE 59(5):1157–1163. https://doi.org/10.13031/trans.59.11726
63. Zhang N, Arroyo M, Cianta MO, Gens A, Butlanska J (2019) Standard penetration testing in a virtual calibration chamber. Comput Geotech 111:277–289. https://doi.org/10.1016/j.compgeo.2019.03.021
64. Zhang N, Evans TM. Three dimensional discrete element method simulations of interface shear. Soils and foundations. 2018 Aug 1;58(4):941-5 https://doi.org/10.1016/j.sandf.2018.05.010
65. Zhong, W., Liu, H., Wang, Q., Zhang, W., Li, Y., Ding, X. and Chen, L., 2021. Investigation of the penetration characteristics of snake skin–inspired pile using DEM. Acta Geotechnica, 16(6):1849–1865. https://doi.org/10.1007/s11440–020–01132–2

List of Captions

Figure 1. DEM simulation model. (a) Simulated probe and virtual calibration chamber, and (b) measurement spheres in the r–z plane.

Figure 2. Results of triaxial compression simulations. Evolution of (a) deviatoric stress, (b) stress ratio, and (c) volumetric strain with axial strain.

Figure 3. Schematic of (a) probes with single and dual anchors and (b) the three stages of the DEM simulations. Note that the arrows acting against the probe represent the stresses and forces acting on it. (c) Logic trees of displacement–controlled and force-limited motion algorithms.

Figure 4. Profiles of (a) tip resistance and (b) sleeve friction and (c) soil behavior type classification based on measurements during the cone penetration (CP) stage.

Figure 5. Evolution of (a–d) radial anchor forces and (e–h) tip resistances for two single–anchor probes with anchor lengths of $2D_{probe}$ and $4D_{probe}$ (simulations #1 and #2) and for two dual–anchor probes with spacings of $1D_{probe}$ and $6D_{probe}$ (simulations #4 and #9) during the anchor expansion (AE) stage.

Figure 6. Particle displacement maps at the end of anchor expansion (AE) stage for (a–b) two single–anchor probes with lengths of $2D_{probe}$ and $4D_{probe}$ (simulations #1 and #2) and (c–f) four dual–anchor probes with spacings varying from $1D_{probe}$ to $6D_{probe}$ (simulations #4, #5, #7, #9).

Figure 7. Change in soil stresses at the end of the anchor expansion (AE) stage. (a–d) Radial stresses, and (e–h) vertical stresses for single–anchor probe H4L4EM0.5_D (simulation #2) and dual–anchor probes H4S1EM0.5_D (simulation #4), H4S4EM0.5_D (simulation #7), and H4S6EM0.5_D (simulation #9).

Figure 8. Forces at the end of the anchor expansion (AE) stage: (a–b) radial forces on the top anchor, (c–d) radial forces on the bottom anchor, and (e–f) tip resistance with increasing spacing for probes with different anchor–tip distance and expansion magnitude (simulations #3–#21).

Figure 9. Evolution of (a–d) total reaction and resistance forces and (e–h) component reaction and resistance forces during the tip advancement (TA) stage for single–anchor and dual–anchor probes (note: simulations are displacement–controlled).

Figure 10. Component (a and b) and total reaction forces (c) mobilized at the end of the tip advancement (TA) stage by probes with dual anchors with varying inter–anchor spacing (simulations #3–#9). Note: dashed lines provide values for probes with one anchor (simulations #1 and #2).

Figure 11. Particle displacements at the end of tip advancement (TA) stage for (a–b) two single–anchor probes with anchor lengths of $2D_{probe}$ and $4D_{probe}$ (simulations #2 and #1) and (c–f) four dual–anchor probes with spacings varying from $1D_{probe}$ to $6D_{probe}$ (simulations #4, #5, #7, #9).

Figure 12. Change in soil stresses at the end of the tip advancement (TA) stage. (a–d) Radial stresses, and (e–h) vertical stresses for single–anchor probe H4L4EM0.5_D (simulation #2) and dual–anchor probes H4S1EM0.5_D (simulation #4), H4S4EM0.5_D (simulation #7), and H4S6EM0.5_D (simulation #9).

Figure 13. Forces at the end of the displacement–controlled tip advancement (TA) stage: (a–b) friction forces on the top anchor, (c–d) end bearing forces on the top anchor, and (e–f) tip resistance force with increasing spacing for probes with different anchor–tip distance (simulations #3–#21).

Figure 14. Ratios of total reaction force to total resistance force at the end of the tip advancement (TA) stage for displacement–controlled simulations on probes with dual anchors (simulations #3–#21).

Figure 15. Tip advancement (TA) displacement ΔD for probes with different (a) expansion magnitudes (simulations #27, #29, #30), (b) anchor–tip distances (simulations #27, #28, #31), and (c) anchor spacings (simulations #23, #27, #35, #36) for force-limited simulations.

Figure 16. Tip advancement ability as a function of probe configuration (simulations #2–#49) for probes with anchor length (L) of $2D_{probe}$ (note: D refers to displacement-control motion and F refers to the force-limited motion).

Table 1. DEM simulation parameters.

Table 2. List of DEM simulations.

Table 3. Particle size effect on the measurements of single-anchor probe with $L=2D_{probe}$.

Table 1. DEM simulation parameters.

Input Parameter	Symbol	Value
Normal Stiffness to Particle Diameter (N/m^2)	k_n/d	1.00E+08
Normal to Shear Stiffness Ratio for Particles	k_n/k_s	1.5
Normal Stiffness of Probe (N/m)	k_{np}	1.42E+07
Shear Stiffness of Probe (N/m)	k_{np}/k_{sp}	9.47E+06
Sliding Friction Coefficient	μ	0.4
Rolling Friction Coefficient	μ_{rr}	0.4
Ball–anchor Friction Coefficient	μ_p	0.3
Ball–wall Friction Coefficient	μ'	0.1
Particle Density (kg/m^3)	G_s	2650

Table 2. List of DEM simulations.

Parameter	#	Name	L/D_{probe}	S/D_{probe}	H/D_{probe}	EM	Number of Anchors	Control Algorithm
Single Anchor	1	H4L2EM0.5_D	2	0	4	0.5	1	DC
	2	H4L4EM0.5_D	4	0	4	0.5	1	DC
Spacing for $H = 4D_{probe}$	3	H4S0.5EM0.5_D	2	0.5	4	0.5	2	DC
	4	H4S1EM0.5_D		1				
	5	H4S2EM0.5_D		2				
	6	H4S3EM0.5_D		3				
	7	H4S4EM0.5_D		4				
	8	H4S5EM0.5_D		5				
	9	H4S6EM0.5_D		6				
Spacing for $H = 1D_{probe}$	10	H1S1EM0.5_D	2	1	1	0.5	2	DC
	11	H1S2EM0.5_D		2				
	12	H1S4EM0.5_D		4				
	13	H1S6EM0.5_D		6				
Spacing for $EM = 0.3$	14	H4S1EM0.3_D	2	1	4	0.3	2	DC
	15	H4S2EM0.3_D		2				
	16	H4S4EM0.3_D		4				
	17	H4S6EM0.3_D		6				
Spacing for $EM = 0.7$	18	H4S1EM0.7_D	2	1	4	0.7	2	DC
	19	H4S2EM0.7_D		2				
	20	H4S4EM0.7_D		4				
	21	H4S6EM0.7_D		6				
Force–limited motion for $S = 1D_{probe}$	22	H4S1EM0.5_F	2	1	4	0.5	2	VC
	23	H1S1EM0.5_F			1	0.5		
	24	H4S1EM0.3_F			4	0.3		
	25	H4S1EM0.7_F			4	0.7		
	26	H2.5S1EM0.5_F			2.5	0.5		
Force–limited motion for $S = 4D_{probe}$	27	H4S4EM0.5_F	2	4	4	0.5	2	VC
	28	H1S4EM0.5_F			1	0.5		
	29	H4S4EM0.3_F			4	0.3		
	30	H4S4EM0.7_F			4	0.7		
	31	H2.5S4EM0.5_F			2.5	0.5		
Additional force-limited motion for characterizing critical plane (Figure 17)	32	H1L4EM0.5_F	4	0	1	0.5	1	VC
	33	H2L4EM0.5_F			2			
	34	H3L4EM0.5_F			3			
	35	H4L4EM0.5_F			4			
	36	H4S6EM0.5_F	2	6	4	0.5	2	
	37	H2.5S2EM0.5_F		2	2.5			
	38	H1S1EM0.3_F	2	1	1	0.3	2	
	39	H1S4EM0.3_F		4	1			
	40	H2.5S1EM0.3_F		1	2.5			
	41	H2.5S4EM0.3_F		4	2.5			
Additional displacement–controlled motion for characterizing critical plane (Figure 17)	42	H1S1EM0.3_D	2	1	1	0.3	2	DC
	43	H1S4EM0.3_D		4	1			
	44	H2.5S1EM0.3_D		1	2.5			
	45	H2.5S4EM0.3_D		4	2.5			
	46	H2.5S1EM0.5_D	2	1	2.5	0.5	2	
	47	H2.5S2EM0.5_D		2				
	48	H2.5S4EM0.5_D		4				
	49	H2.5S6EM0.5_D		6				
Particle Size	50	H4L2EM0.5_D-R	2	0	4	0.5	1	DC

*Note: L is anchor length, S is spacing between the two anchors, H is the distance between the anchor and the tip, EM is the anchor expansion magnitude, and D is the probe diameter; D and F represent displacement–controlled and force-limited motion, respectively.

Table 3. Particle size effect on the measurements of single-anchor probe with $L=2D_{probe}$.

Specimen	D_{50} (mm)	CP stage		AE stage		TA stage	
		q_c (MPa)	f_s (kPa)	F_n (kN)	Q_c (kN)	F_t (kN)	Q_t (kN)
Original	14.2	4.8	30.0	16.5	6.1	5.5	7.6
Particle refinement	6.3	5.2	34.1	18.9	6.6	6.1	8.5

Note: the CP measurements (q_c and f_s) are averaged from 0.2 to 0.55 m soil depth; the AE and TA measurements (F_n, Q_c, F_t, Q_t) are the end values of each stage; the TA stage is displacement controlled (DC).

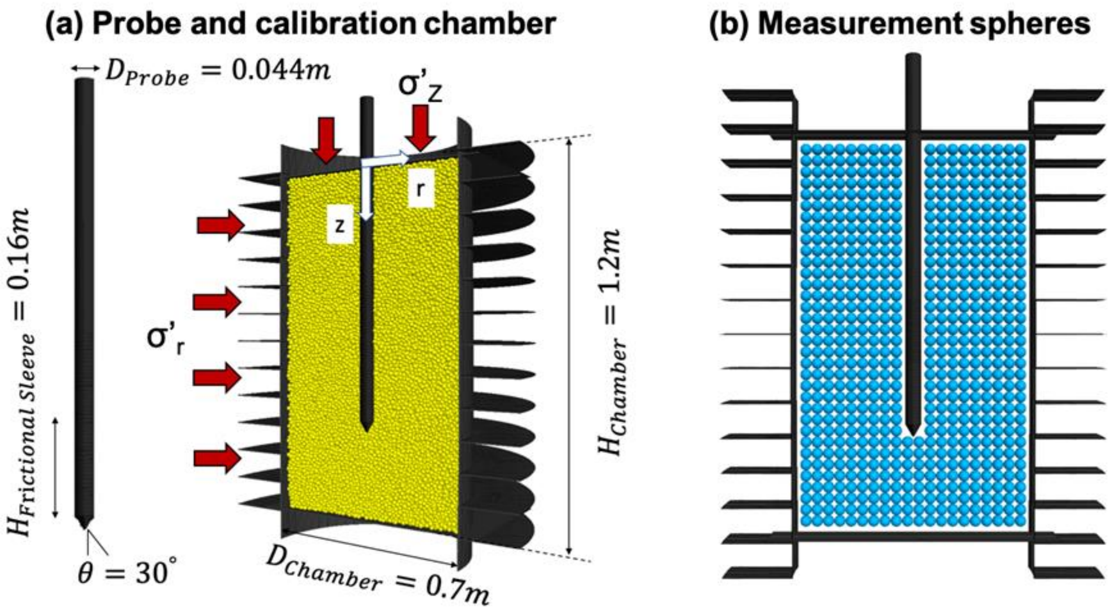

Figure 1. DEM simulation model. (a) Simulated probe and virtual calibration chamber, and (b) measurement spheres in the r–z plane.

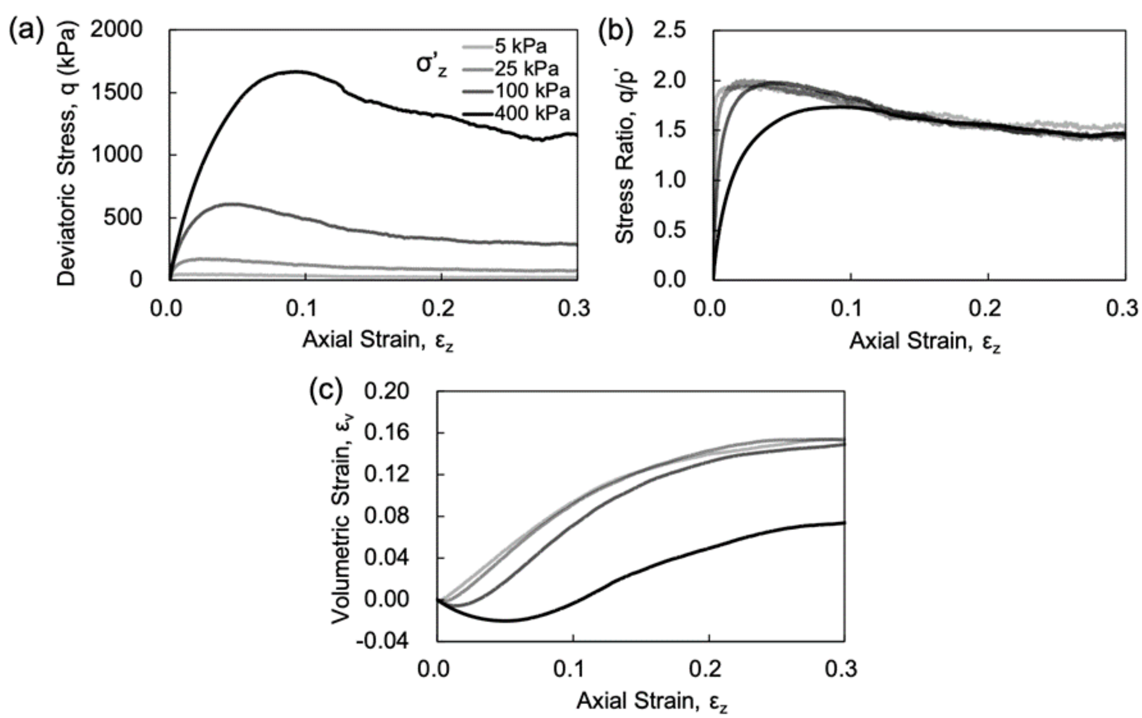

Figure 2. Results of triaxial compression simulations. Evolution of (a) deviatoric stress, (b) stress ratio, and (c) volumetric strain with axial strain.

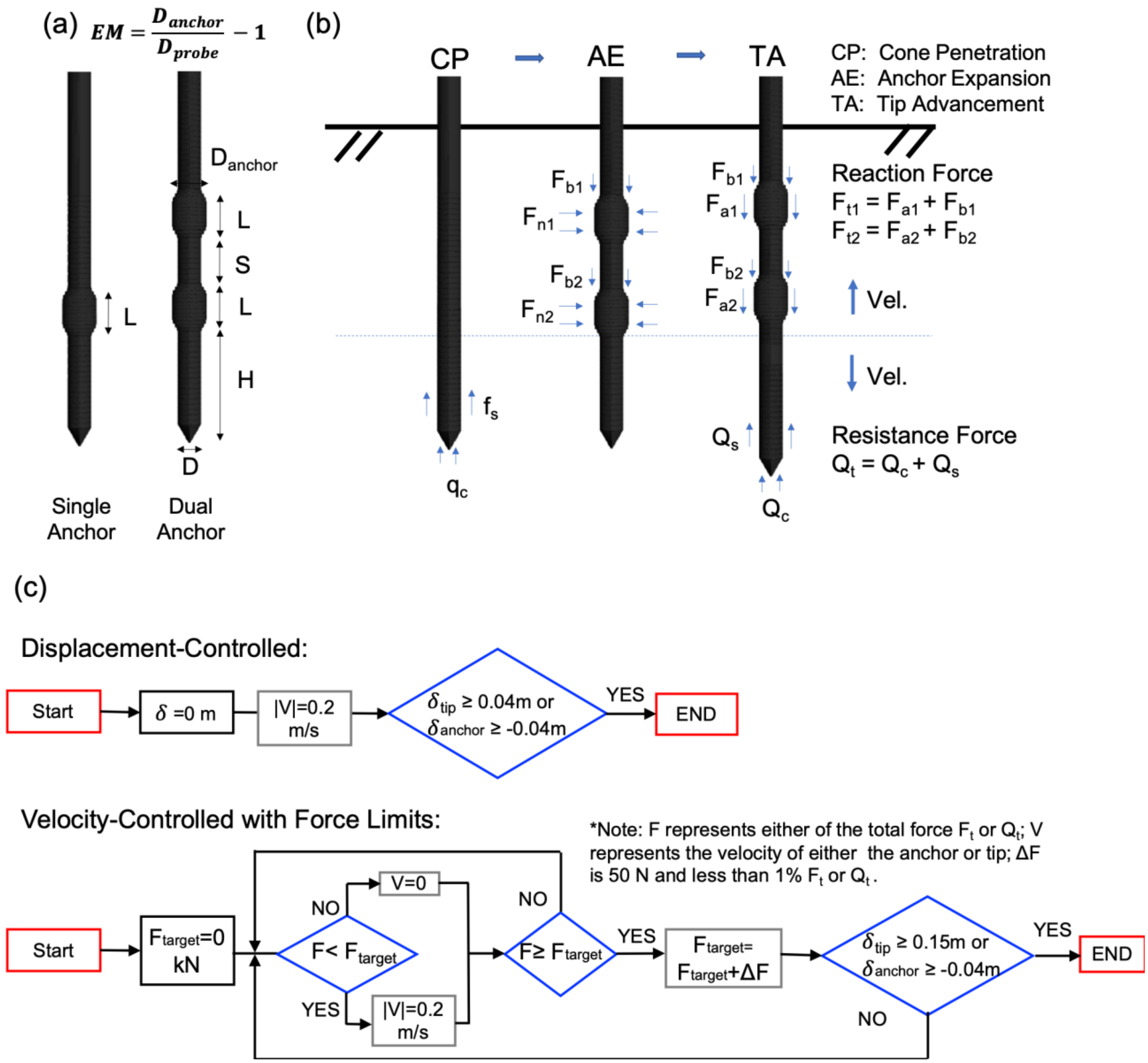

Figure 3. Schematic of (a) probes with single and dual anchors and (b) the three stages of the DEM simulations. Note that the arrows acting against the probe represent the stresses and forces acting on it. (c) Logic trees of displacement–controlled and force-limited probe motion algorithms.

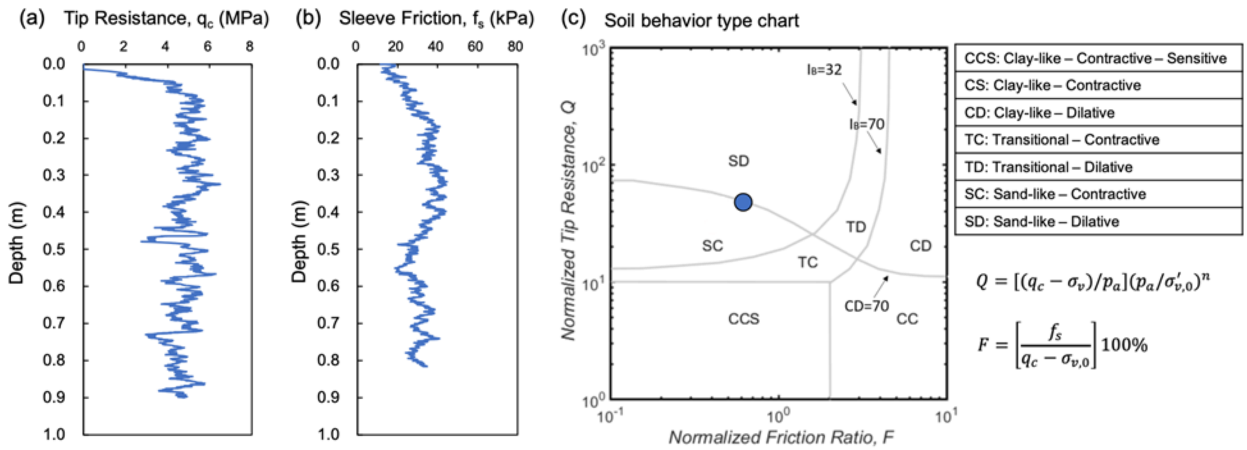

Figure 4. Profiles of (a) tip resistance and (b) sleeve friction and (c) soil behavior type classification based on measurements during the cone penetration (CP) stage.

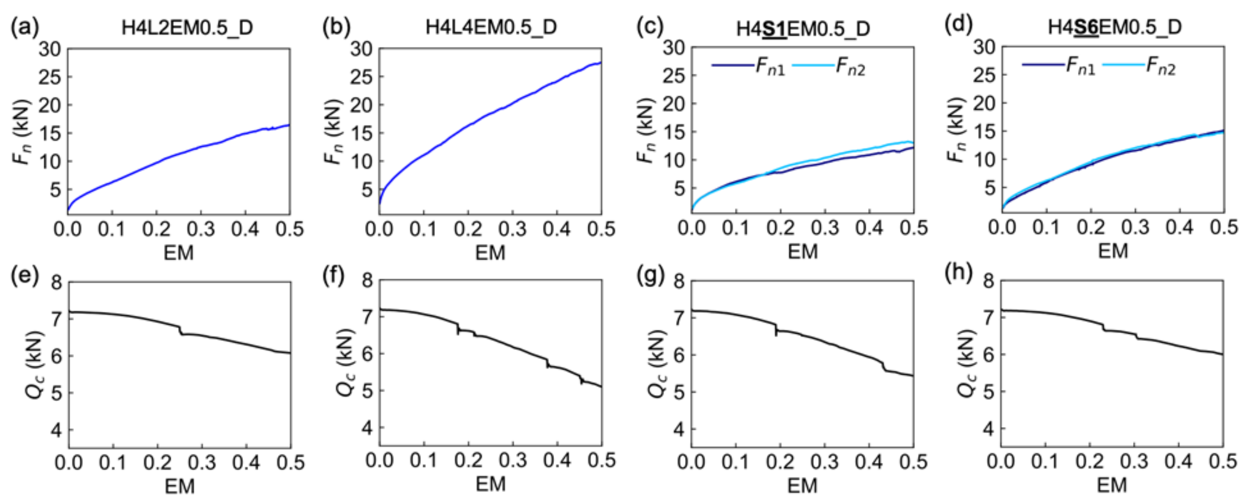

Figure 5. Evolution of (a–d) radial anchor forces and (e–h) tip resistances for two single–anchor probes with anchor lengths of $2D_{probe}$ and $4D_{probe}$ (simulations #1 and #2) and for two dual–anchor probes with spacings of $1D_{probe}$ and $6D_{probe}$ (simulations #4 and #9) during the anchor expansion (AE) stage.

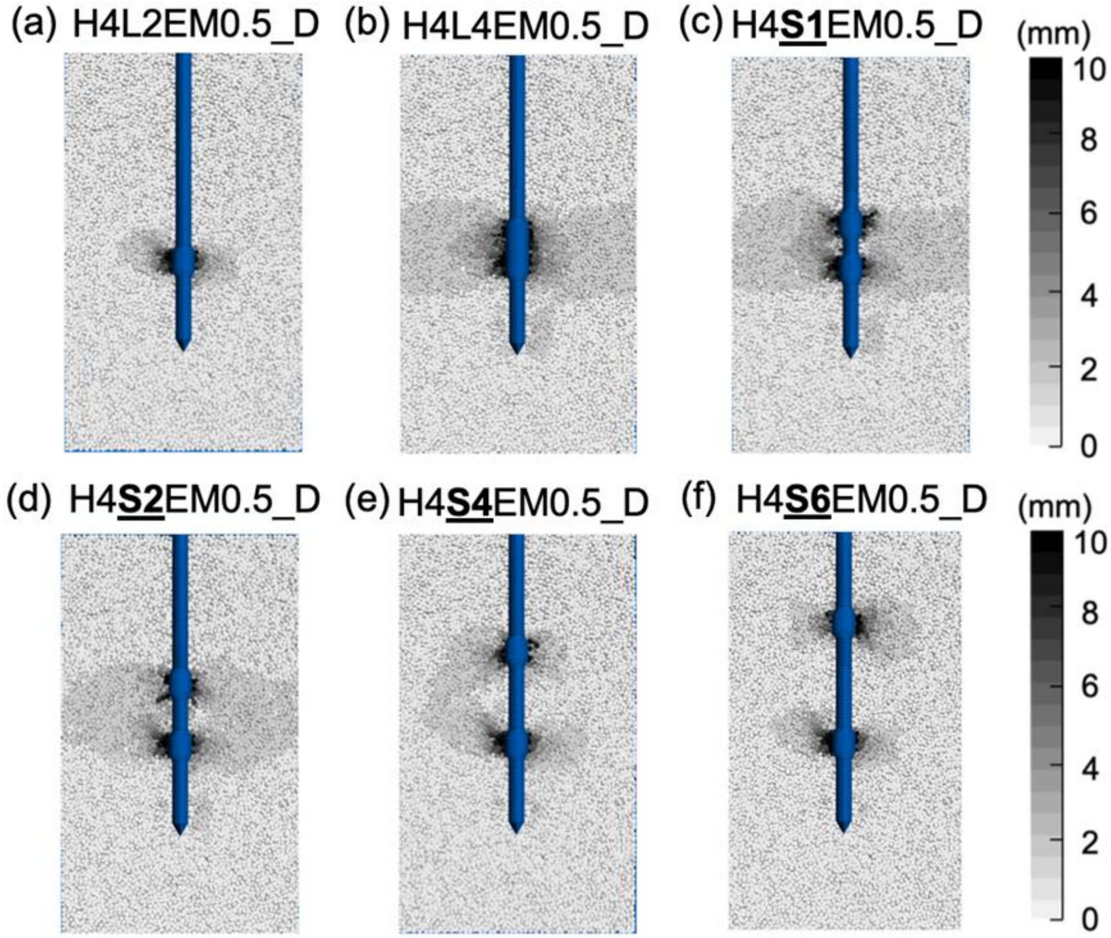

Figure 6. Particle displacement maps at the end of anchor expansion (AE) stage for (a–b) two single–anchor probes with lengths of $2D_{probe}$ and $4D_{probe}$ (simulations #1 and #2) and (c–f) four dual–anchor probes with spacings varying from $1D_{probe}$ to $6D_{probe}$ (simulations #4, #5, #7, #9).

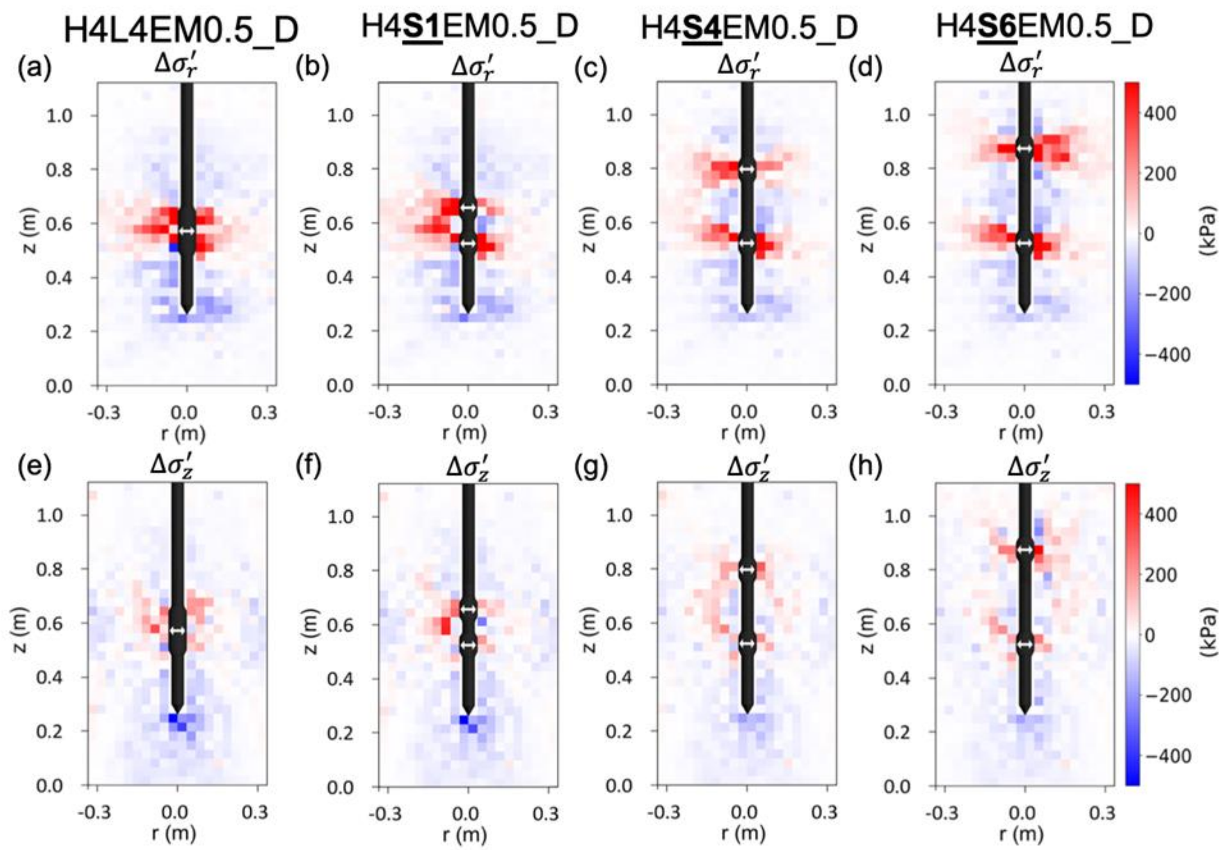

Figure 7. Change in soil stresses at the end of the anchor expansion (AE) stage. (a–d) Radial stresses, and (e–h) vertical stresses for single–anchor probe H4L4EM0.5_D (simulation #2) and dual–anchor probes H4S1EM0.5_D (simulation #4), H4S4EM0.5_D (simulation #7), and H4S6EM0.5_D (simulation #9).

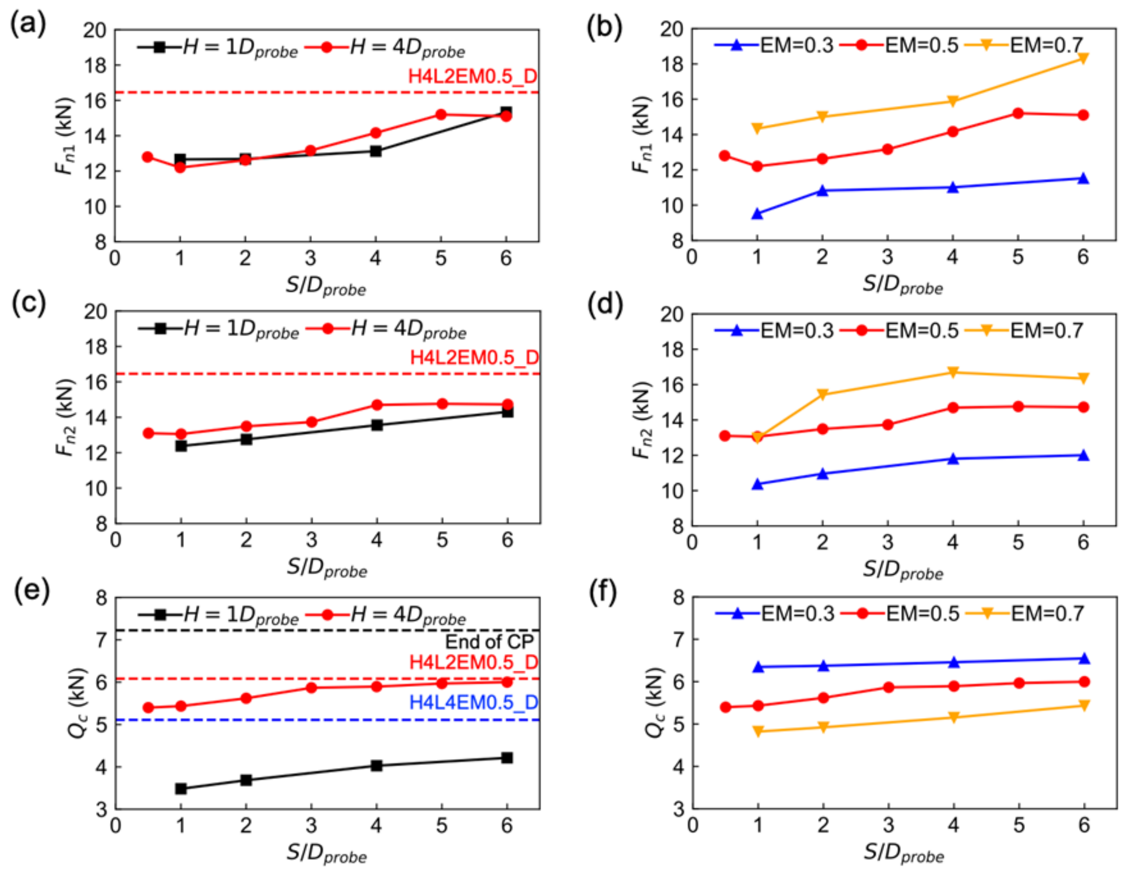

Figure 8. Forces at the end of the anchor expansion (AE) stage: (a–b) radial forces on the top anchor, (c–d) radial forces on the bottom anchor, and (e–f) tip resistance with increasing spacing for probes with different anchor–tip distance and expansion magnitude (simulations #3–#21).

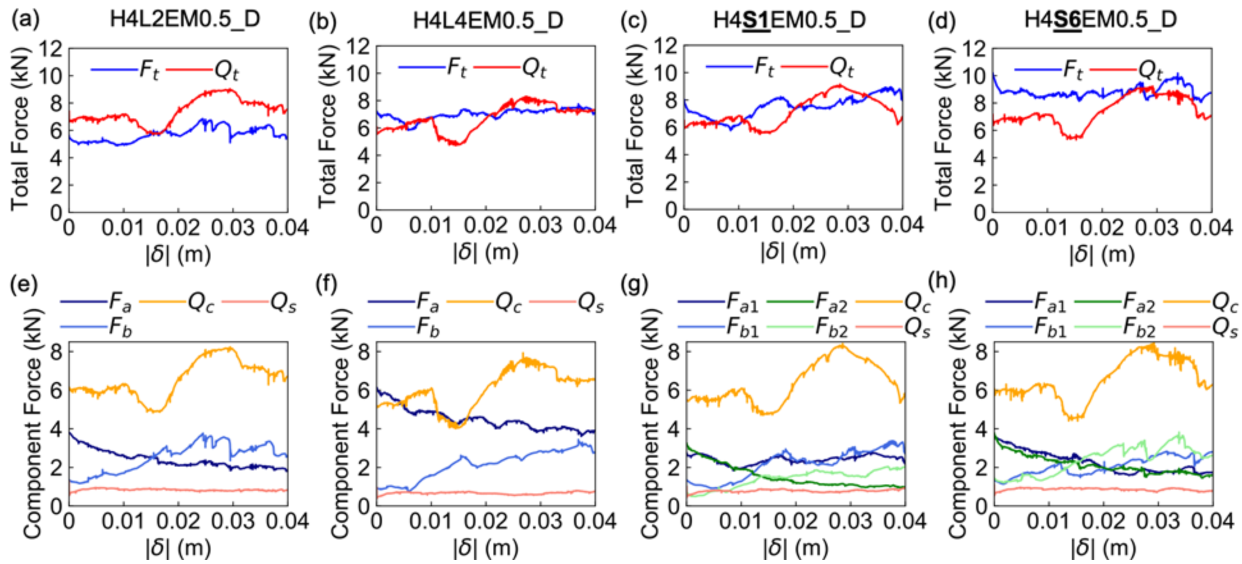

Figure 9. Evolution of (a–d) total reaction and resistance forces and (e–h) component reaction and resistance forces during the tip advancement (TA) stage for single–anchor and dual–anchor probes (note: simulations are displacement–controlled).

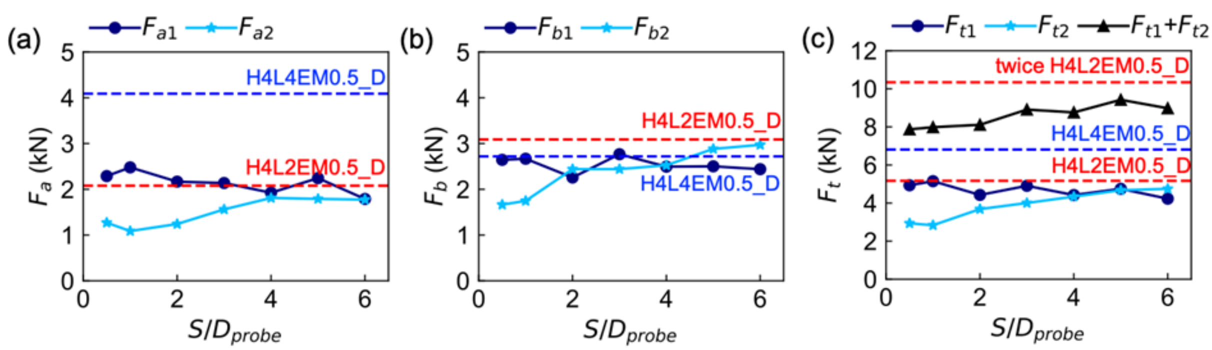

Figure 10. Component (a and b) and total reaction forces (c) mobilized at the end of the tip advancement (TA) stage by probes with dual anchors with varying inter–anchor spacing (simulations #3–#9). Note: dashed lines provide values for probes with one anchor (simulations #1 and #2).

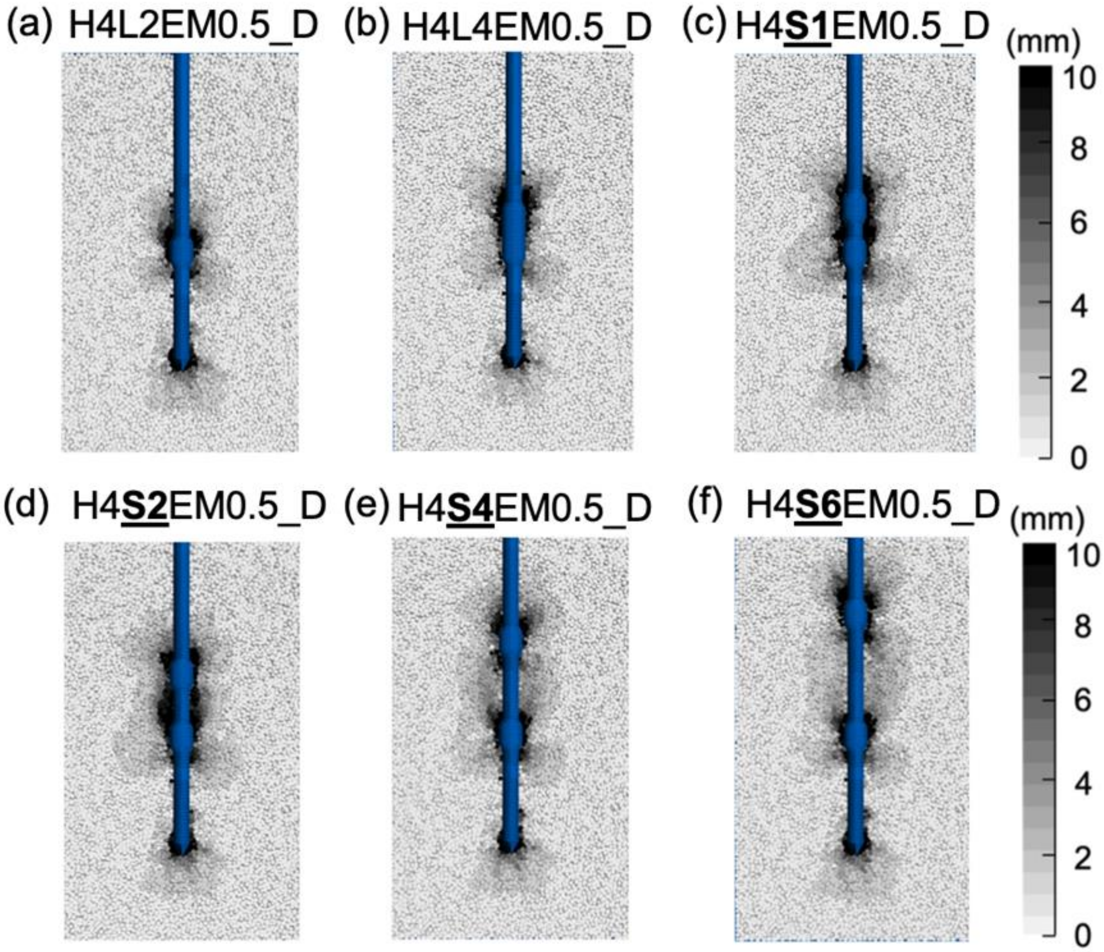

Figure 11. Particle displacements at the end of tip advancement (TA) stage for (a–b) two single–anchor probes with anchor lengths of $2D_{probe}$ and $4D_{probe}$ (simulations #2 and #1) and (c–f) four dual–anchor probes with spacings varying from $1D_{probe}$ to $6D_{probe}$ (simulations #4, #5, #7, #9).

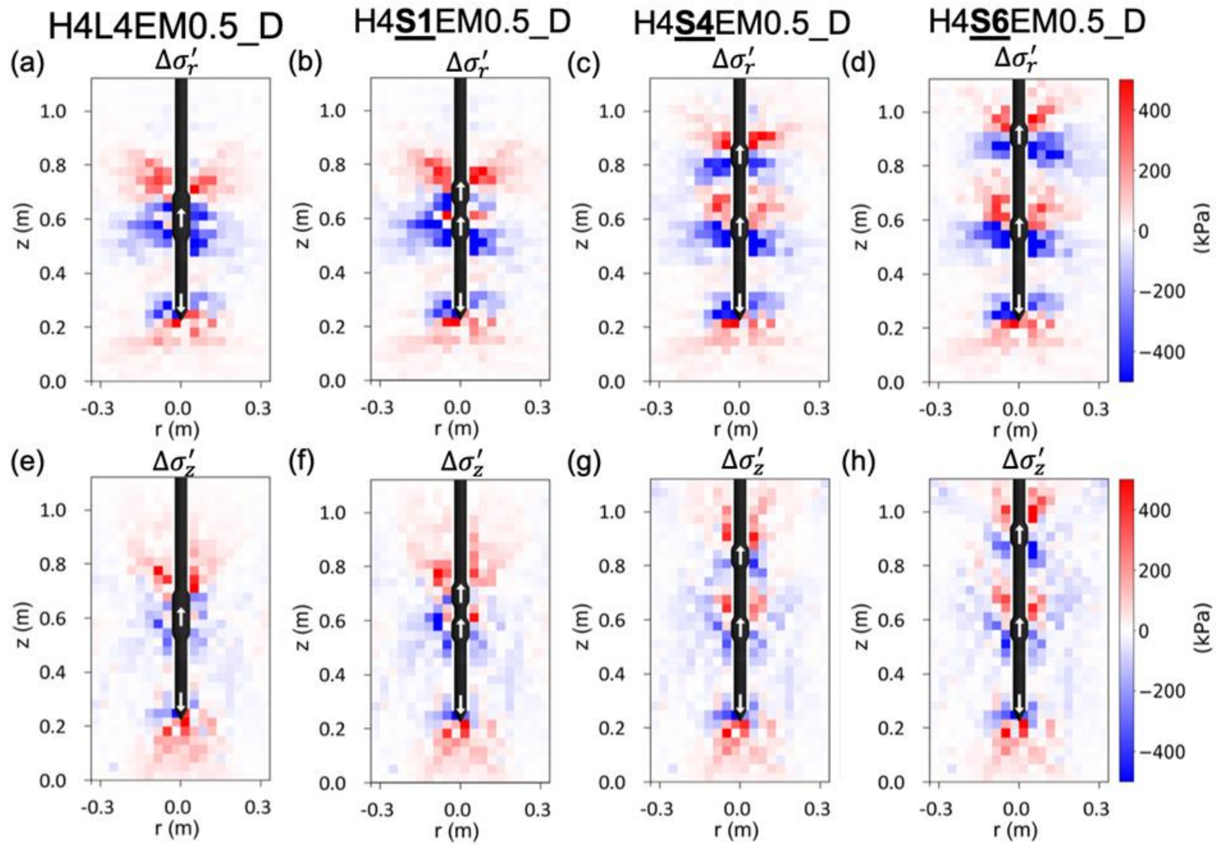

Figure 12. Change in soil stresses at the end of the tip advancement (TA) stage. (a–d) Radial stresses, and (e–h) vertical stresses for single–anchor probe H4L4EM0.5_D (simulation #2) and dual–anchor probes H4S1EM0.5_D (simulation #4), H4S4EM0.5_D (simulation #7), and H4S6EM0.5_D (simulation #9).

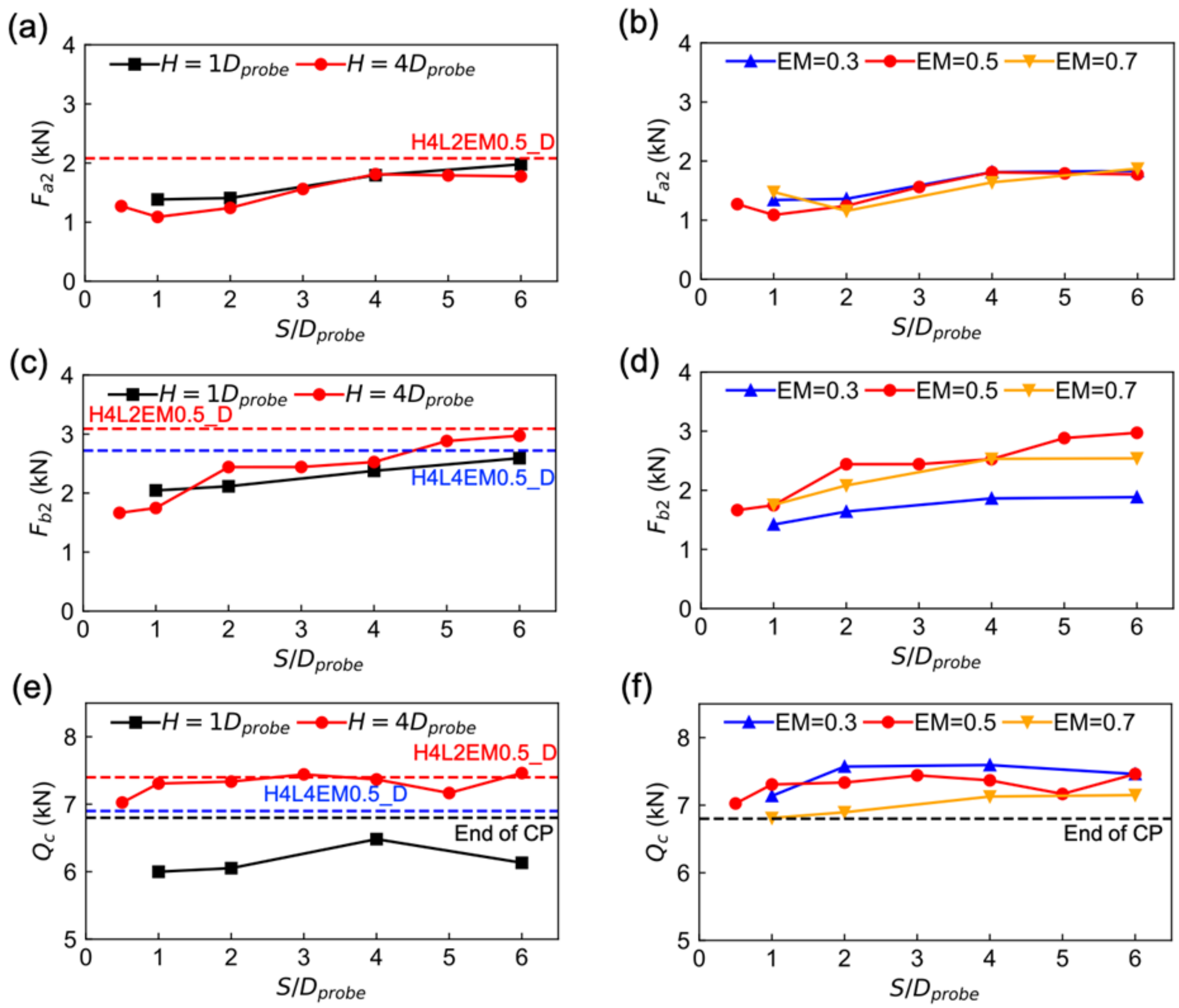

Figure 13. Forces at the end of the displacement–controlled tip advancement (TA) stage: (a–b) friction forces on the top anchor, (c–d) end bearing forces on the top anchor, and (e–f) tip resistance force with increasing spacing for probes with different anchor–tip distance (simulations #3–#21).

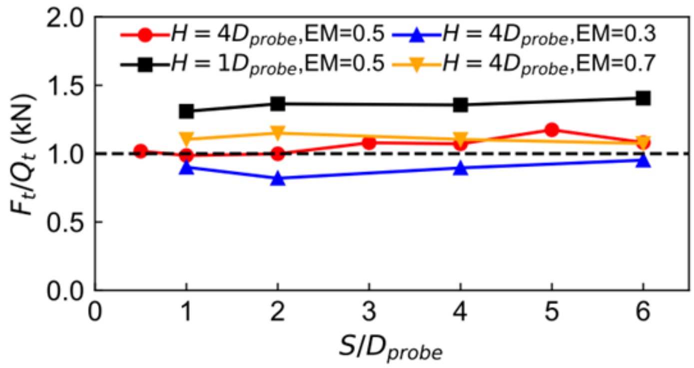

Figure 14. Ratios of total reaction force to total resistance force at the end of the tip advancement (TA) stage for displacement–controlled simulations on probes with dual anchors (simulations #3–#21).

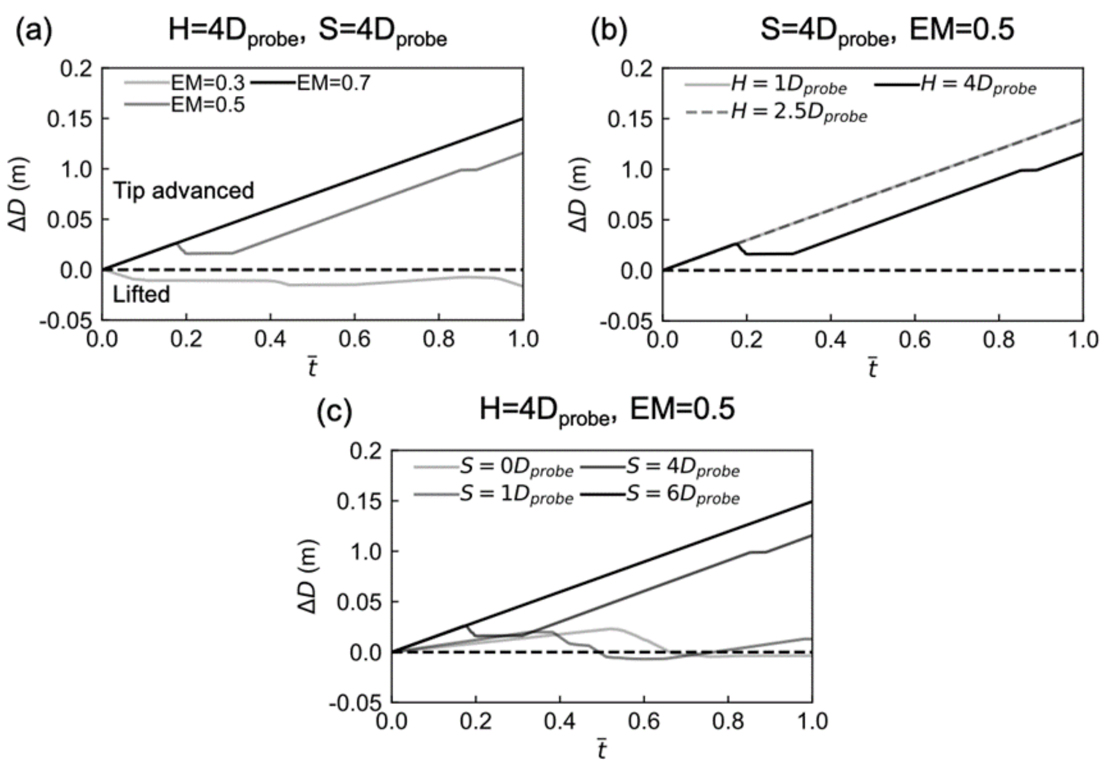

Figure 15. Tip advancement (TA) displacement for probes with different (a) expansion magnitudes (simulations #27, #29, #30), (b) anchor–tip distances (simulations #27, #28, #31), and (c) anchor spacings (simulations #23, #27, #35, #36) for force-limited simulations.

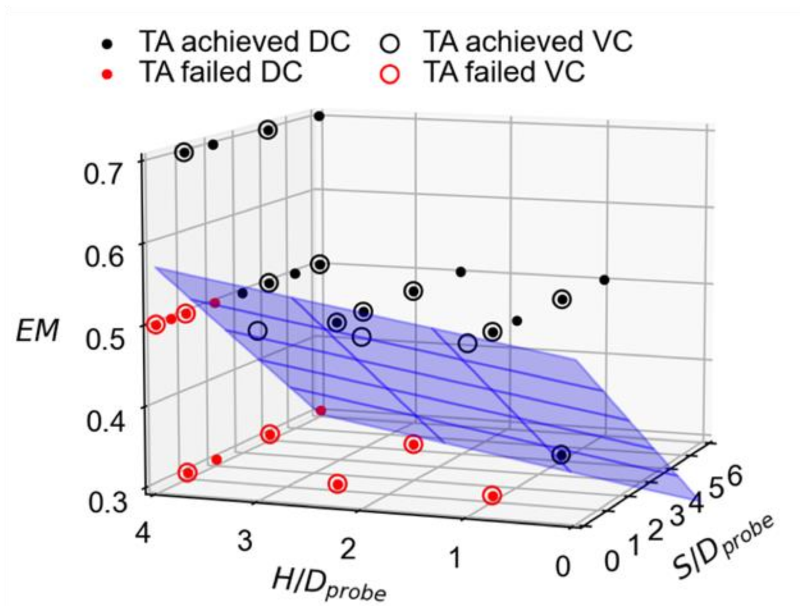

Critical Plane: $EM = -0.046 * S/D_{probe} + 0.020 * H/D_{probe} + 0.488$

Figure 16. Tip advancement ability as a function of probe configuration (simulations #2–#49) for probes with anchor length (L) of $2D_{probe}$ (note: D refers to displacement-control motion and F refers to the force-limited motion).

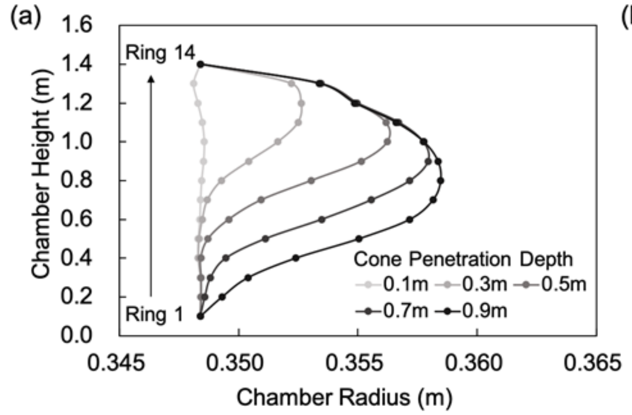

Figure S1. Distribution of (a) chamber radius and (b) chamber stress along the chamber height (note: ring 1 and ring 14 are not in contact with the particles, therefore they are not shown in (b).

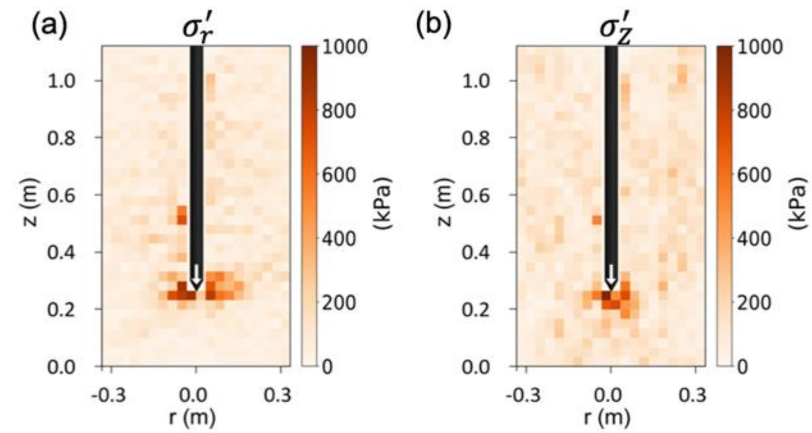

Figure S2. Stresses at the end of cone penetration (CP) stage: (a) radial and (b) vertical soil stresses.

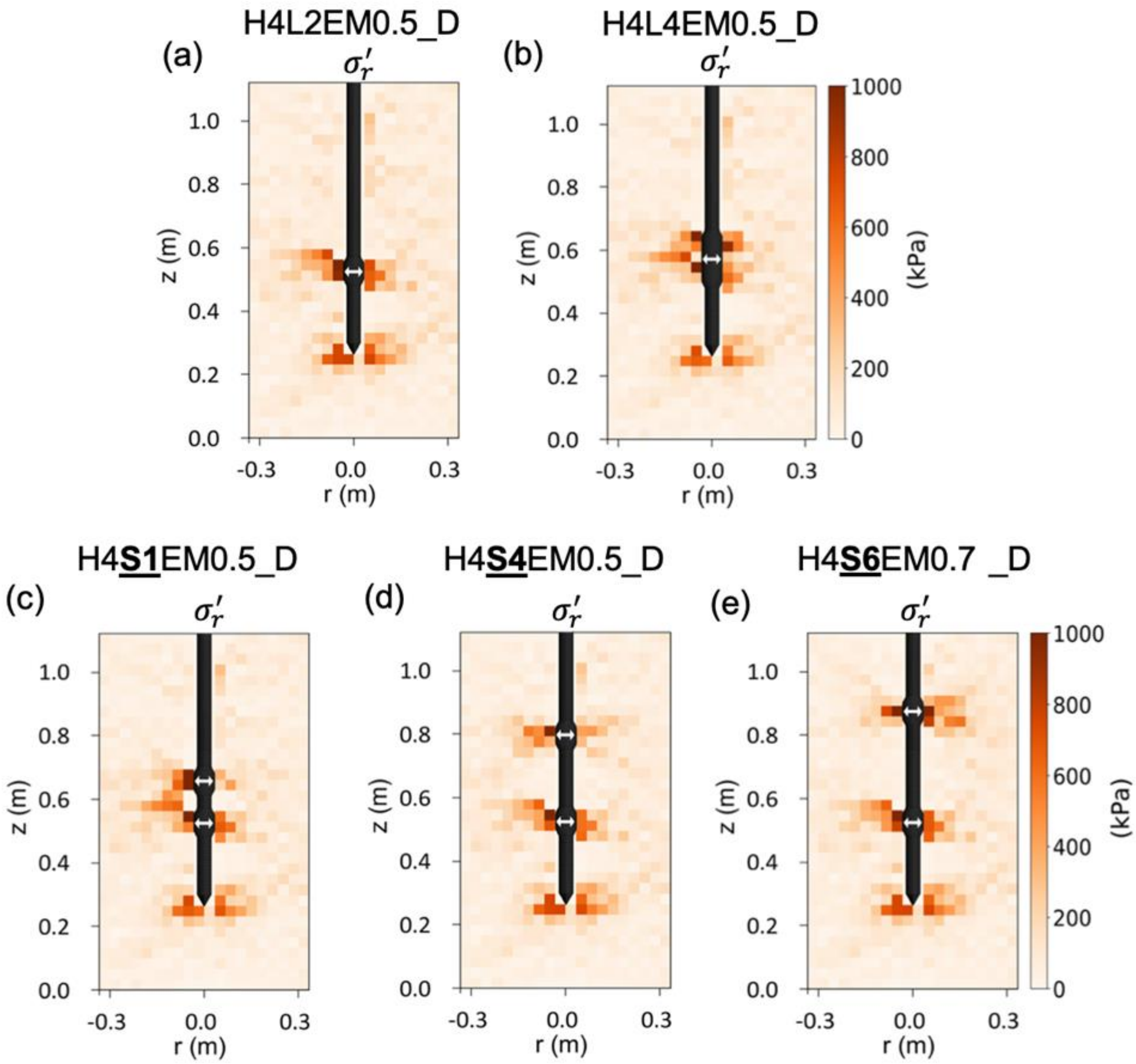

Figure S3. Radial stresses at the end of anchor expansion (AE) stage for probes (a) H4L2EM0.5_D (simulation #1), (b) H4L4EM0.5_D (simulation #2), (c) H4S1EM0.5_D (simulation #4), (d) H4S4EM0.5_D (simulation #7), and (e) H4S6EM0.5_D (simulation #9).

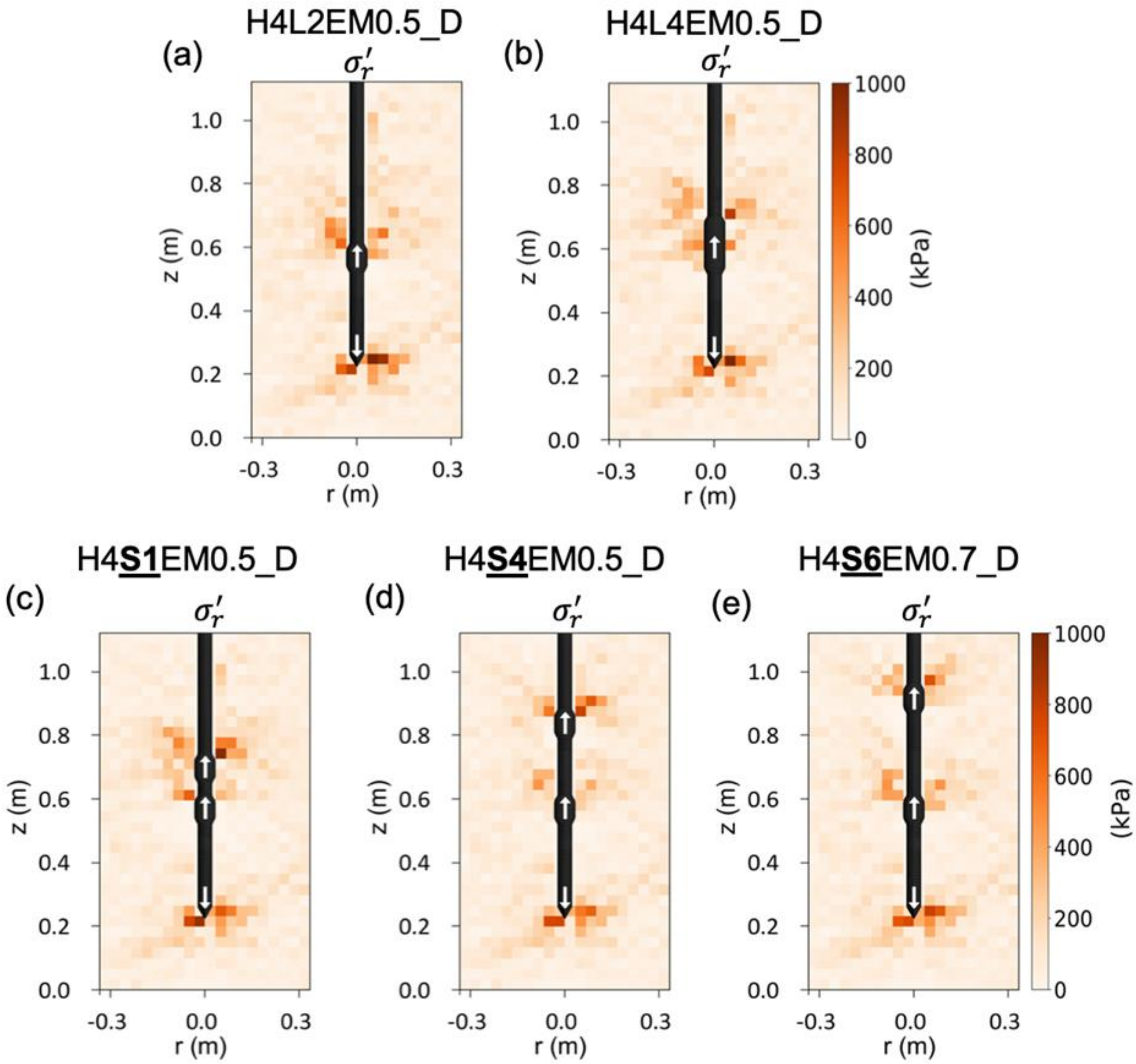

Figure S4. Radial stresses at the end of tip advancement (TA) stage for probes (a) H4L2EM0.5_D (simulation #1), (b) H4L4EM0.5_D (simulation #2), (c) H4S1EM0.5_D (simulation #4), (d) H4S4EM0.5_D (simulation #7), and (e) H4S6EM0.5_D (simulation #9).

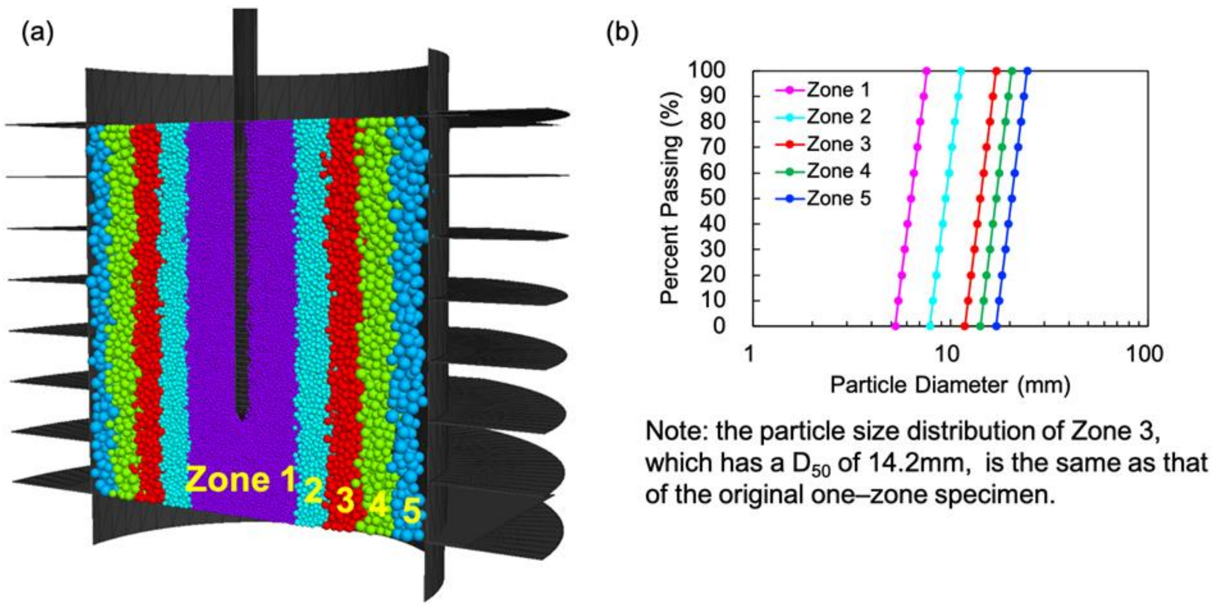

Fig.S5 Soil specimen with particle refinement. (a) Virtual calibration chamber, probe and soil particles; (b) particle size distributions in the 5 zones of the soil sample (with the particle size upscaled by 1.5 and 1.2 for inner three zones and outer three zones, respectively).

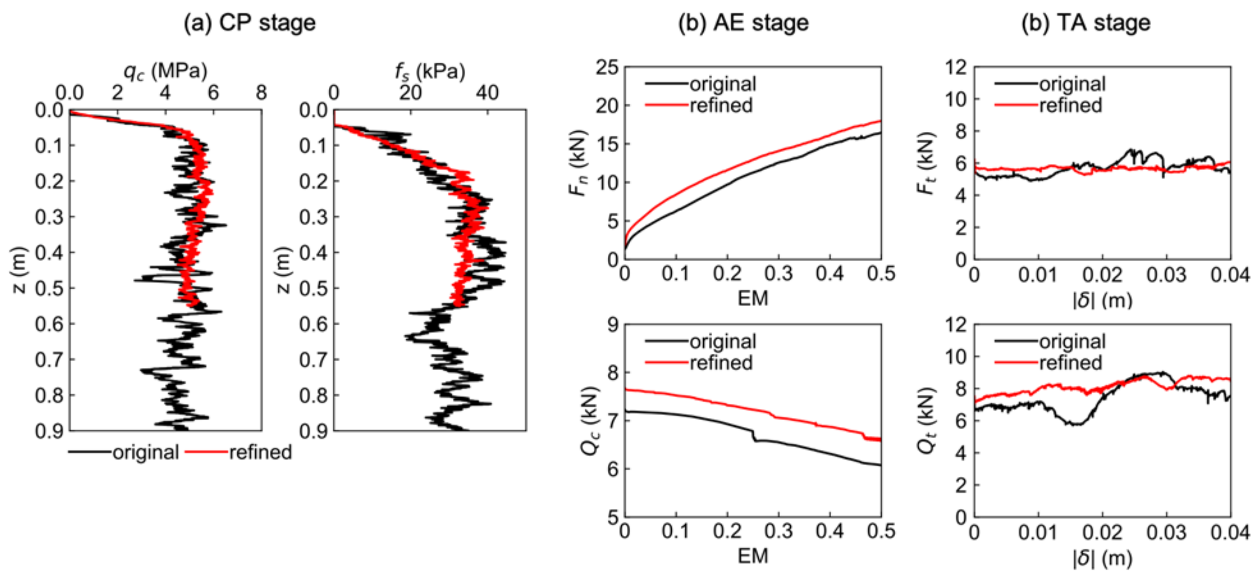

Fig.S6 Comparisons between results of in original specimen and those of specimen with five-zone particle refinement for simulations with a single-anchor probe H4L2. (a) Tip resistance and sleeve friction during the CP stage; (b) radial anchor force and tip force during the AE stage; (b) total reaction force and total resistance force during the TA stage. Note that while the CP stage of the refined specimen ends at 0.55 m depth, the comparisons is valid because the anchor and tip are both located in the region that q_c measurement is stable.